POLITECNICO
MILANO 1863

SCUOLA DI INGEGNERIA INDUSTRIALE
E DELL'INFORMAZIONE

White matter changes in Episodic Migraine: a neurite orientation dispersion and density imaging (NODDI) study.

Tesi di Laurea Magistrale in
Biomedical Engineering - Ingegneria Biomedica

Author: **Dario Del Cuore**

Student ID: 10745578
Advisor: Prof. Anna Maria Maddalena Bianchi
Co-advisors: Prof. Rita Homem de Gouveia Costanzo Nunes, Prof. Patrícia Margarida Piedade Figueiredo
Academic Year: 2022-23

Abstract

Nowadays, Migraine could be classified as an intense pulsatile painful neurological condition, characterized by the presence of several headaches attacks in a span of three months (not more than 14 headaches for Episodic Migraineurs, more than 14 episodes for Chronic Migraneiurs). In particular, this work was centered on the analysis of Menstrual Migraine, which is a type of Episodic Migraine where migraine attacks directly relate to the menstruation period of the subject. Neuroimaging has been extensively used to characterize brain changes in migraine patients but there are still not many effective therapeutic plans against this type of disease. For this reason, the analysis of the white-matter alterations was still considered a challenge by the whole scientific community. The purpose of this work is to detect white matter alterations in Episodic Migraine patients by the use of diffusion MRI. Particularly, the neurite orientation dispersion and density imaging (NODDI) model has been applied. NODDI is a model of the signal measured with diffusion-weighted MRI, which differs from other more common models (like Diffusion Tensor Imaging or Diffusion Kurtosis Imaging) by its capability of providing quantitative compartment-specific metrics. Thus, with NODDI is possible to provide the contribution given by the singular tissue components, showing what influence the singular tissues have in the final image. The data collected from a group of 14 control subjects and 9 menstrual migraineurs was analyzed with the application of the NODDI model followed by a TBSS analysis. The acquisition of the controls has been performed for two conditions: premenstrual (before the start of the menstrual cycle) and midcycle (during the menstrual cycle). Regarding the episodic migraineurs, the acquisition has been performed in four different conditions: interictal (in between two different seizures), preictal (before the start of the seizure), ictal (during the seizure), and postictal (after the seizure). Relevant white-matter alterations were found in the left inferior fronto-occipital fasciculus (p-value=0.048), left forceps major (p-value=0.028), left superior longitudinal fasciculus (p-value=0.040), and left cingulum (p-value=0.038) for the ISOVF (Isotropic Volume Fraction) parameter in the comparison between midcycle phase (controls) and interictal phase (Episodic Migraine patients). No relevant results were found for the parameters ICVF (Intracellular Volume Fraction) and ODI (Orientation Dispersion Index) in this comparison.

Moreover, the author tried to implement the statistical analysis using the Region-of-interest (ROI) analysis based on the results obtained from the previous TBSS analysis, with the use of the JHU (Johns Hopkins University) white matter atlases, considering a total number of 14 controls and 10 episodic migraineurs. The ROI analysis has been applied to 10 ROIs in total, obtaining significant differences between controls and migraineurs in the left splenium of corpus callosum (uncorrected p-value=0.01766), left anterior thalamic radiation (uncorrected p-value=0.01535), left posterior corona radiata (uncorrected p-value=0.02696), left inferior fronto-occipital fasciculus (uncorrected p-value=0.04392) and left superior longitudinal fasciculus (uncorrected p-value=0.02871) for the ISOVF (Isotropic Volume Fraction) parameter. It has been possible to state that the results that were found with the ROI analysis has shown consistency just for the left inferior fronto-occipital fasciculus compared to the previous TBSS analysis.
Generally, the availability of a small sample size related to the specific migraine phases could be seen as a strong limitation of the present study. Indeed, a large dataset should be required in order to investigate deeply the alteration of the whole-brain white-matter tracts in menstrual migraine. Moreover, it was not fully certain that the NODDI model should be the most suitable one for the case of episodic migraine.

Keywords: White Matter Alteration, Migraine, Episodic Migraine, Menstrual Migraine, MRI, DWI, NODDI, AMICO.

Abstract in lingua italiana

L'emicrania è definita come una condizione neurologica caratterizzata dalla presenza di numerosi attacchi di cefalea nell'arco di tre mesi (non più di 14 episodi per l'emicrania episodica, più di 14 episodi per l'emicrania cronica) di grave entità dolorosa e a carattere pulsante. In particolare, questo lavoro è stato incentrato sull'analisi dell'emicrania mestruale, la quale è un tipo di emicrania episodica in cui gli attacchi di emicrania sono direttamente correlati al periodo mestruale del soggetto. Varie tecniche di neuroimagiologia sono state ampiamente utilizzate per caratterizzare le modifiche cerebrali nei pazienti con emicrania, ma non ci sono ancora protocolli terapeutici del tutto efficaci contro questo tipo di malattia. Per tale motivo, l'analisi delle alterazioni della sostanza bianca è ancora considerata una sfida da tutta la comunità scientifica. Lo scopo di questo studio è rilevare le alterazioni della sostanza bianca nei pazienti con emicrania episodica mediante l'uso della risonanza magnetica di diffusione. In particolare, è stato applicato il modello NODDI (neurite orientation dispersion and density imaging). NODDI è un modello di segnale misurato con la risonanza magnetica pesata in diffusione, che differisce da altri modelli più comuni (come Diffusion Tensor Imaging o Diffusion Kurtosis Imaging) per la sua capacità di fornire metriche quantitative specifiche dei singoli compartimenti presenti nei voxels. Inoltre, con tale metodica è possibile fornire informazioni sul contributo dato dai singoli componenti tissutali, mostrando quale influenza hanno i singoli tessuti nell'immagine finale. I dati raccolti da un gruppo di 14 soggetti di controllo e 9 soggetti con emicrania mestruale sono stati analizzati con l'applicazione del modello NODDI seguito dalla analisi statistica TBSS. L'acquisizione dei soggetti di controllo è stata effettuata in due condizioni: premestruale (prima dell'inizio del ciclo mestruale) e midcycle (durante il ciclo mestruale). Per quanto riguarda i pazienti con emicrania episodica, l'acquisizione è stata eseguita in quattro diverse condizioni: interictale (tra due diverse crisi), preictale (prima dell'inizio della crisi), ictale (durante la crisi) e postictale (dopo la crisi). Rilevanti alterazioni della sostanza bianca sono state riscontrate nel fascicolo fronto-occipitale inferiore sinistro (p-value=0,048), forcipe maggiore sinistro (p-value=0,028), fascicolo longitudinale superiore sinistro (valore p=0,040) e cingolo sinistro (p-value=0.038) per il parametro ISOVF (Isotropic Volume Fraction) nel confronto

tra la fase midcycle (soggetti di controllo) e la fase interictale (pazienti con emicrania episodica). In questo confronto non sono stati trovati risultati rilevanti per i parametri ICVF (Intracellular Volume Fraction) e ODI (Orientation Dispersion Index).
Inoltre, l'autore ha cercato di implementare l'analisi statistica utilizzando l'analisi della regione di interesse (ROI) basata sui risultati ottenuti dalla precedente analisi TBSS, con l'utilizzo degli JHU (Johns Hopkins University) white matter atlases, considerando un totale numero di 14 controlli e 10 emicranici episodici. L'analisi ROI è stata applicata a 10 ROIs in totale, ottenendo differenze significative tra i soggetti di controllo e i pazienti con emicrania nello splenio sinistro del corpo calloso (uncorrected p-value=0,01766), radiazione talamica anteriore sinistra (uncorrected p-value=0,01535), corona radiata (uncorrected p-value = 0,02696), fascicolo fronto-occipitale inferiore sinistro (uncorrected p-value = 0,04392) e fascicolo longitudinale superiore sinistro (uncorrected p-value = 0,02871) per il parametro ISOVF (isotropic volume fraction). È stato possibile affermare che i risultati che sono stati trovati con l'analisi ROI hanno mostrato coerenza solo per il fascicolo fronto-occipitale inferiore sinistro comparati alla precedente analisi TBSS.
In generale, la disponibilità di una dataset ridotto potrebbe essere vista come una forte limitazione per il presente studio. Un ampio dataset è richiesto al fine di indagare in profondità sull'alterazione dei tratti di sostanza bianca per l'intero emisfero cerebrale nell'emicrania mestruale. Inoltre, non era del tutto certo che il modello NODDI potrebbe essere il modello più adatto nel caso di emicrania episodica.

Parole chiave: Alterazioni della sostanza bianca, Emicrania, Emicrania Episodica, Emicrania Mestruale, MRI, DWI, NODDI, AMICO.

Contents

1 | Motivation

1.1. The context

Migraine has been classified by the International Classification of Headache Disorders (ICHD), 3rd edition [1], as a recurrent headache disorder with attacks that last 4 to 72 hours. The typical features associated to it are several. For instance, it is possible to mention a pulsating quality, unilateral location, association with nausea and/or phonophobia and photophobia, aggravation by routine physical activity and many more [2]. Nowadays, Migraine headache is considered the third most common disease, globally estimated with a prevalence of 15 %, and it is also included in the top ten debilitating diseases that are causing substantial suffering to the family in addition to the sufferer [3].
Specifically for this case of study, Episodic Migraine (EM) was preferred over Chronic Migraine (CM) due to the fact that it is easier to acquire the data for EM patients than for CM ones. Indeed, the patients that have been considered in the study, Menstrual Migraineurs, showed particular symptoms before the actual seizure, which allowed them to understand the period of time in which they will experience the seizure. Hence, they were aware of the time in which they could go to the laboratory and perform the acquisition and, for this reason, it was possible to collect the data at the moment in which the seizure was starting. Generally, menstruation could be included as one of the most important migraine triggers among female migraineurs. It has been stated that women with a diagnosis of Menstrual Migraine (MM) felt more painful menstrual attacks and most disabling and less responsive treatments [4]. Even if it is an extremely common disease, there are still not many effective therapeutic plans against it. This is partially due to the lack of knowledge of the cause of the disease itself and, for this reason, the investigations on the white-matter alterations are still considered a challenge by the whole scientific community.
Regarding the CM patients, these are subjected to more seizures during the day, but, it is not easy for these types of patients to understand exactly when the seizure will start.

The focus on the in-vivo white matter could help to deepen our understanding of the

disease. In order to assess the pathology in an in vivo and non-invasive manner, sensitive and powerful neuroimaging techniques have been developed. The recent advances in Magnetic Resonance Imaging (MRI) have provided compelling evidence, which is why it's nowadays used to study the majority of brain pathologies. Diffusion Magnetic Resonance Imaging (dMRI) is one of the available MRI techniques that could provide in vivo microstructural information on biological tissues in a non-invasive way and, hence, it has been applied in several studies related to white-matter abnormalities in migraineurs.

White Matter (WM) could be defined as the structural basis of functional integrations between brain regions. The analysis of the intertwining structure-function relationship enlighten by the white matter tracts could provide several insights into the comprehensive process of the cognitive and behavioral impairments in migraineurs patients. It is essential to understand that detecting microstructural abnormalities in the white matter might benefit not only the understanding of abnormal functional activities, but also the earliest detection of the neurodegenerative signs that migraine could cause.
As mentioned, dMRI measures the diffusion of water molecules in the brain and this could easily enlighten the white matter microstructure configurations. Among the dMRI techniques, Diffusion Tensor Imaging (DTI) was one of the first models that have been used to study the white matter microstructure in migraine. One of its limitation, is that the DTI model is not excluding the free-water contributions from the dataset. Indeed, in order to provide biologically meaningful features that are free from contamination due to free water, the scientific community proposed a set of biophysical diffusion models. Particularly, the Neurite Orientation Dispersion and Density Imaging (NODDI) model caught the attention of the author because of its feasibility and simplicity in clinical settings. Indeed, the NODDI model is capable to provide quantitative compartment-specific metrics that are biologically meaningful and interesting from a clinical point of view, including the Free Water Fraction (FWF), also called Isotropic Volume Fraction (ISOVF), which quantifies the extent of contamination caused by Cerebrospinal Fluid (CSF); the Neurite Density Index (NDI), also called Intracellular Volume Fraction (ICVF), which provides an estimate of axonal density in white matter; the Orientation Dispersion Index (ODI), which quantifies the extent of axonal dispersion in white matter. NODDI was already applied in several neurological applications that involved the analysis of white matter lesions, such as in First-episode Psychosis [5], Alzheimer's disease [6], Focal Cortical Dysplasia [7], Epilepsy [7], Parkinson's disease [8] and Huntington's disease [9]. The model had not been previously applied in Migraine research studies.
One clear hypothesis has been made in this work:

- NODDI could detect white matter alterations when comparing between EM patients and control subjects.

Within the aim of testing this hypothesis, the data acquisition of 14 controls and 9 EM patients has been performed, using Tract-Based Spatial Statistics (TBSS) for quantitative analysis. In order to further test this hypothesis and to validate the results obtained with the previous TBSS analysis, in this work a Region of interest (ROI) analysis has been used, considering a total number of 14 controls and 10 EM patients.

1.2. Problem statement and aim of the thesis project

In this work, the author applied the NODDI model to an already existing dataset of controls and MM patients. By taking advantages of the complexity of the NODDI model, the author is aiming to find new lesions in the WM of MM patients that were not discovered in previous DTI or Diffusion Kurtosis Imaging (DKI) studies in order to increase the potential understanding of the causes of Migraine. Additionally, it could also be possible to improve our understanding in the brain areas in which WM alterations have been already found. This could be also important to test the suitability of the NODDI model for the specific disease that has been considered.

1.3. Structure of the thesis

The rest of the thesis has been organized as explained below:

Chapter 2 - this chapter provides a general description of the diffusion MRI (dMRI) techniques, including the basics of water diffusion, how to measure water diffusion using MRI and how to analyze diffusion MRI images using NODDI.

Chapter 3 - in this chapter, it is possible to find an accurate description of the white matter microstructure in the human brain and a general definition of migraine.

Chapter 4 - this chapter establishes the application of NODDI's model in EM patients, describing the dataset, image acquisition, framework and type of statistical analysis that have been used for our purposes.

Chapter 5 - this chapter shows the results that have been obtained by the depiction of the in-vivo WM pathology for migraine disease.

Chapter 6 - in this chapter it is possible to find a summary of all the key findings, within the discussion of the results for both TBSS analysis and ROI analysis.

Chapter 7 - this chapter shows all the potential limitations associated to the NODDI model and to the study itself, suggesting potential work in the future.

2 | Diffusion Magnetic Resonance Imaging

This chapter has been created with the aim of offering an introduction to the basic principles behind dMRI. In subchapter 2.1, the basic physical phenomenon of water diffusion is described. Then, in order to understand what is the principal role of MRI in the measurement of water diffusion, subchapter 2.2 is included. At the end of the chapter, it is explained how to computationally obtain tissue microstructural information by the use of dMRI models. Indeed, in subchapter 2.3, the DTI is introduced. In subchapter 2.4, the NODDI (Neurite orientation dispersion and density imaging) is explained, including its mathematical description, fitting techniques, and metrics. Subchapter 2.5 explain the main differences between DTI and NODDI, englightening the limitations that DTI could present compared to NODDI. Finally, in subchapter 2.6, all the techniques related to image analysis for dMRI are explained.

2.1. Water Diffusion

2.1.1. Free Diffusion vs Restricted Diffusion

In order to enlighten the differences between these types of diffusion, the definition of Brownian motion is essential. This is the random, uncontrolled movement of particles in a fluid as they constantly collide with other molecules, caused by their thermal energy [10]. The Brownian movement was first discovered by Robert Brown in his observation of the movements of pollen grains via micro-scope, in 1827 [11].

Regarding free diffusion, this can be characterized by the probability of finding a particle at a certain position after a defined diffusion time. Giving an example, free diffusion is the phenomenon of the dispersion of the ink molecules into an infinitive space covered by water. This is defined as “free” because there is no physical barrier that is limiting the diffusion process. Indeed, it is possible to state that the displacement of the singular

particle is directly proportional to the diffusion time only, just because there is no barrier that is limiting the movement of the particle.

In restricted diffusion, instead, there are spatial barriers that are blocking the diffusion of the particles in a specific area. For instance, the water diffusion inside the cell membrane could be considered a restricted diffusion, because of the presence of a physical barrier that can influence the phenomenon itself. Indeed, the relationship between the displacement and the diffusion time is not linear in this case. This is due to the fact that it has been observed that the estimated diffusion value is changing for each experiment depending on the diffusion time. Thus, the diffusion constant can't be considered as a constant value (as it was in free diffusion), but its value depends on the diffusion time.

2.1.2. Einstein equation

The Einstein equation is the one that linked the Fick's laws to the self diffusion phenomenon, with the aim of clearly explaining the mechanism of molecular diffusion [12] (Equation 2.1):

$$< r^2 >= 6Dt. \tag{2.1}$$

According to Einstein equation, the mean squared displacement of molecules (r^2) is directly proportional to the diffusion time t, through the diffusion coefficient D. It is important to bear in mind that the diffusion coefficient D depends on the size of the molecules, viscosity of medium and temperature [13] (Equation 2.2):

$$D = \frac{k_B T}{6\eta\pi\sigma}, \tag{2.2}$$

where k_B is the Boltzmann constant, T is the temperature, η is the viscosity and σ is the radius of the particle.
The aforementioned formulation for the mean squared displacement of molecules is referred to as the free diffusion only, in which D is effectively constant.
In the restricted diffusion case, the diffusion coefficient is not constant anymore and it will depend on diffusion time, as mentioned before. Hence, the formulation could be re-written in this way:

$$< r^2 >= 6D(t)t, \tag{2.3}$$

in which D is defined as an apparent diffusion coefficient (ADC).

2.1.3. Non-invasively examination of the brain microstructure using Water Diffusion.

As mentioned before, in a free space, the molecules are diffusing randomly and freely along any direction due to thermal energy. Although, by taking into account everything that has been stated so far for the restricted diffusion, barriers reduce the velocity of the molecules that come across them. Hence, molecular diffusion is less limited along the direction that is parallel to the barriers than the ones that are perpendicular to them.
From what has been stated, it is possible to understand the direction of the movements of water molecules, which is directly correlated to the spatial structure of a sampled material, through the analysis of the velocity of the molecules.
It is crucial to take into account that, in MRI, water molecules are the ones that are targeted due to their abundance in the biological tissue. As mentioned before, the diffusion displacement of water molecules is affected by the presence of biological barriers, such as the aforementioned cell membrane. Hence, the distribution of the water diffusion could reflect the underlying microstructural configurations of the tissue [14]. In conclusion, it is possible to infer the in vivo microstructural information of the biological tissue in a non-invasive way by the measurement of water diffusion.

2.1.4. Water Diffusion in CSF, Gray Matter and White Matter.

The three main tissues present in the brain are Gray Matter (GM), White Matter (WM), and Cerebrospinal Fluid (CSF). Depending on their structures, each of them has different configurations of barriers for water diffusion. Figure 2.1 shows the different configurations for the three types of tissues.

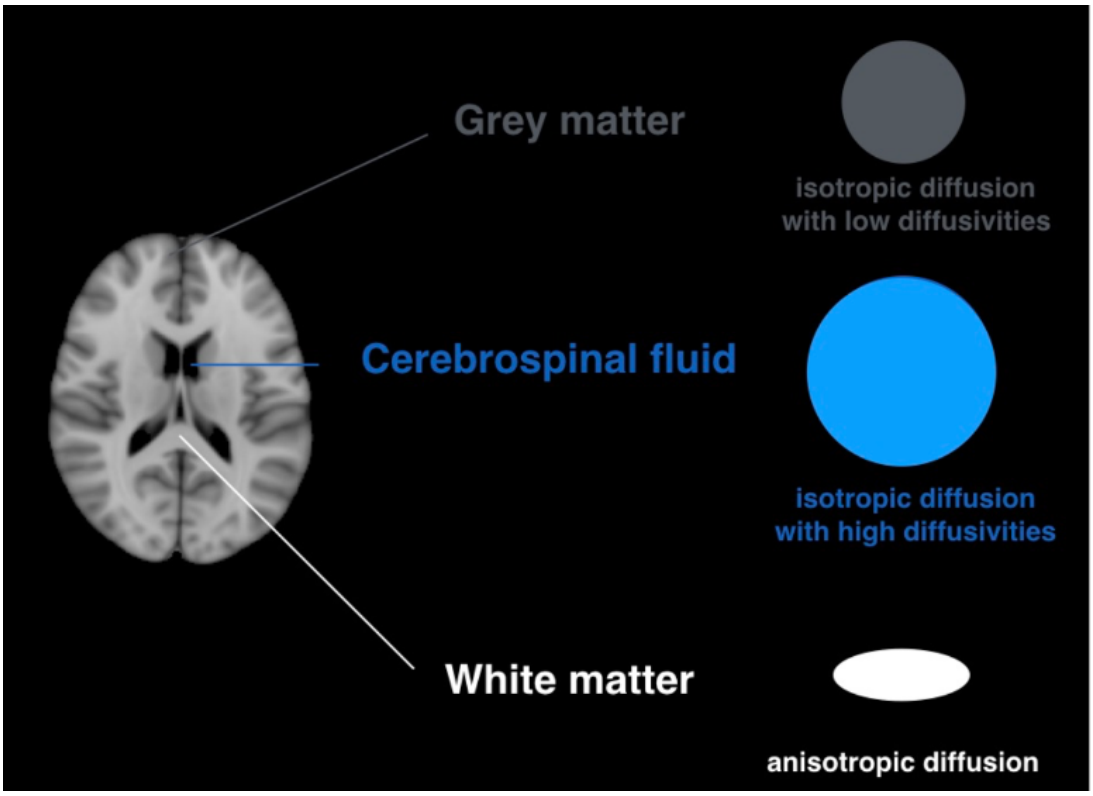

Figure 2.1: Microstructure configuration of White matter, Gray matter, and cerebrospinal fluid within their diffusion conditions. The figure has been taken from [15]

.

Starting from the CSF, water molecules are diffusing freely in any direction due to the fact that there is no barrier that is blocking the movement. Thus, the water diffusion in CSF is isotropic with a high diffusivity. Regarding the GM, this is mainly composed of dendrites and neuronal cell bodies. Cell membranes represent an obstacle to water diffusion and, for this reason, the diffusivity is lower, compared to CSF. Even though in GM, water diffusion does not present orientation preferences. Hence, the diffusion is still isotropic. Taking into account the WM instead, this is often referred to as the fiber tracts and includes mainly the myelinated axons. Here, the water molecules are diffusing freely along the direction of the fiber. While, the diffusion is highly restricted in the direction that is perpendicular to the fiber. Therefore, in this case, it is possible to visualize an orientation preference and, for this reason, the diffusion is considered anisotropic.

2.2. Measuring water diffusion in the tissue using MRI

2.2.1. MRI Introduction

MRI has been used clinically for more than 30 years. Nowadays, MRI serves as the primary diagnostic modality for many clinical problems. Starting from the early 1980s, MRI has revolutionized the diagnostic and treatment process of several medical conditions [16]. Indeed, over the past 30 years, different magnetic resonance techniques (such as novel hardware components or new pulse sequence acquisition strategies) have been processed in order to shorten the required time for the image acquisition, improve the quality of the image and facilitate advanced anatomic and functional imaging.
It is essential to consider that MRI is based on on the quantum phenomenon called Nuclear Magnetic Resonance (NMR). This is a spectroscopic technique that is used to characterize the spin state of an active nucleus under the influence of a strong magnetic field [17]. Generally, this phenomenon refers to the process of absorbing and re-emitting the energy of protons. NMR was first described by Isidor Isaac Rabi in 1938, who received the 1944 Nobel Prize in Physics [16]. Actually, NMR has been translated into modern MRI systems through the framework of spatial encoding using magnetic field gradients, introduced firstly by Lauterbur et al [18].

Basic NMR concepts

It is crucial to bear in mind that a proton that rotates around its own axis forms a spin $\vec{J}$. One property that is related with the spin $\vec{J}$ is the magnetic moment $\vec{\mu}$, which is determined by

$$\vec{\mu} = \gamma \vec{J},$$

where γ represents the gyromagnetic ratio of the nucleus.
Within the application of a strong external magnetic field $\vec{B_0}$, the torque produced by the external magnetic field will force the magnetic moments to precess and form a non-null net magnetization vector $\vec{M}$ along the direction of the magnetic field. According to the convention, the z-axis is defined as the orientation of the external static magnetic field $\vec{B_0}$, which corresponds to the "longitudinal" axis. The "transverse" axes, instead, define the xy plane.
It is important to notice that when the net-magnetization is parallel to $\vec{B_0}$, this means that the longitudinal magnetization is maximum, while the transverse magnetization is null.
As mentioned before, the application of the external magnetic field will create a magnetic moment precess and the frequency of this movement is called Larmor frequency ω_0. This is defined by the following equation:

$$\omega_0 = \gamma |\vec{B_0}|, \tag{2.4}$$

where $\vec{B_0}$ is the external field and is the gyromagnetic ratio of the nucleus of a particle. Usually, for water molecules, the Larmor frequency is assumed to be 128 MHz with a 3T applied magnetic field.

Required alterations of the system to detect the net magnetization

The application of an external magnetic field will cause the production of a net magnetization vector M_L which is just longitudinal (same direction of application of the magnetic field, z-axes for convention). Although, in order to obtain a sufficient level of signal, induction is needed. This requires a change of $\vec{M}$ in time. For this reason, it is necessary to rotate 90° the magnetization vector, in order to be able to measure the magnetic field through the measurement of signal intensity. Within the application of a Radiofrequency pulse (RF) (Figure 2.2, left), it is possible to flip the magnetization vector onto the xy plane (transverse magnetization M_T). Indeed, during this process, the changing of the magnetization induces electric currents and a measurable signal intensity. It is important to bear in mind that the purpose of MRI is detecting differences throughout different types of tissues, in order to be able to detect possible alterations, medical conditions, or pathologies. It is possible to visualize these differences by the analysis of the relaxation processes along the longitudinal and transversal directions (Figure 2.2, right).

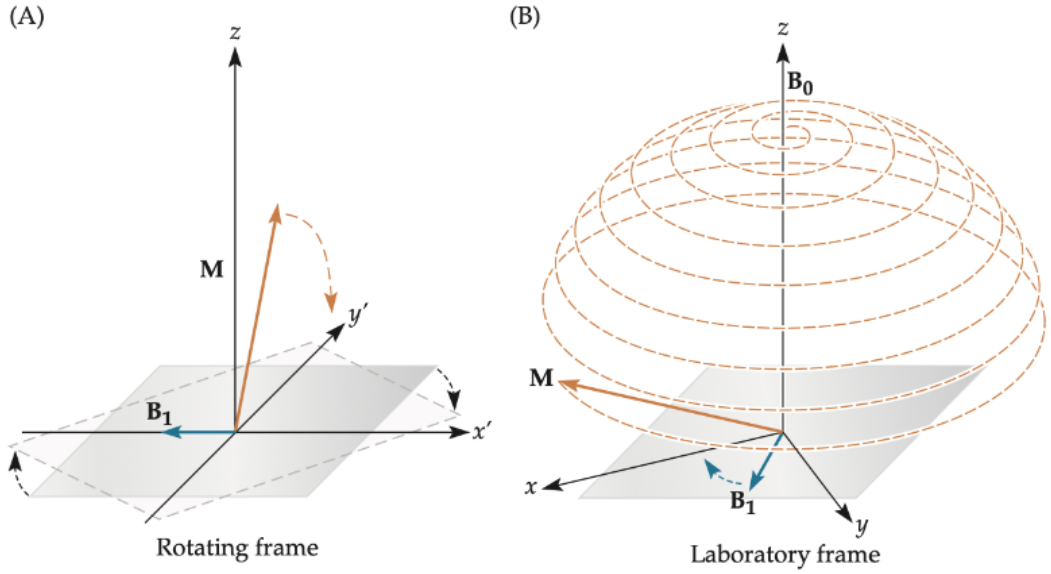

Figure 2.2: The delivery of an excitation pulse ($\vec{B}_1$) causes the longitudinal magnetization ($\vec{M}$) to be flipped onto the transverse plane (xy plane). In A it is possible to visualize the flip of the magnetization vector into the xy plane caused by the application of an RF pulse (that produces the magnetic field $\vec{B}_1$ in the figure). In B it is possible to visualize the relaxation process, in which the magnetization vector is coming back to its original state. However, the longitudinal magnetization will trace out a path that is rotating towards the z-axes. This wobbling motion is also known as nutation. The figure has been selected from [19].

Indeed, when the coil that is producing the RF pulse is turned off, the protons start losing energy gradually and the magnetization vector will return to its basic state (M_T will tend towards to zero, while M_L will return to its original value). In this process, two mechanisms of relaxation (longitudinal and transversal) exist, as it has been stated before.

The longitudinal relaxation is also called **Spin-lattice relaxation** (Figure 2.3, left). As mentioned before, in order to return to the original condition, the release of energy that the spins accumulated when the RF pulse has been applied is needed. Thus, this relaxation represents the transfer of energy from the spins to the "lattice", which includes all the surroundings that will receive that energy as heat [20]. The time constant that represents this type of relaxation is called T1, which is the time required to recover 63% of the original longitudinal magnetization (assuming that a 90° excitation pulse has been applied).

The transverse relaxation, instead, is also called **Spin-spin relaxation** (Figure 2.3, right). This relaxation occurs through a redistribution of energy among various spins of the system [20]. It could be defined as well as a dephasing of the spin rotations around the z-axis. The time constant in this relaxation is called T2 and it represents the time required to lose 37% of the maximum transverse magnetization obtained after the application of the RF pulse.

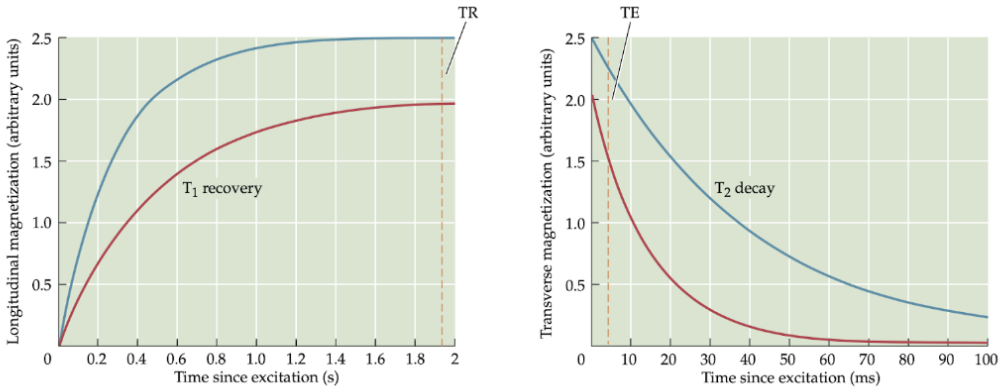

Figure 2.3: Representation of the longitudinal relaxation process (left) and the transversal relaxation process (right) of two different tissues (red and blue curves), assuming that a 90° RF pulse has been applied to excite the sample. The spin-lattice relaxation presents a time constant T1, while the spin-spin relaxation presents a time constant T2. The selection of specific Echo Time (TE) and Repetition Time (TR) are needed in order to make the images sensitive to T1 or T2 (T1 weighted imaging or T2 weighted imaging). The figure has been selected from [19].

Actually, the aforementioned time constant T2 does not fully describe what is observed. In a practical MRI system, when an external magnetic field is applied, the sample will react to this through the production of a small amount of magnetic field, due to the magnetic susceptibility. Thus, the magnetic field won't be considered homogeneous because of the additional dephasing mechanism introduced by the magnetic susceptibility effect. The decay of transverse magnetization is determined by the time constant T2*, which is shorter than the aforementioned T2. Indeed, T2* can be mathematically described by the following formulation:

$$\frac{1}{T2^*} = \frac{1}{T2} + \frac{1}{T2'}, \tag{2.5}$$

where T2' is the time contribution given by the effect of the magnetic susceptibility. In

order to overcome this problem, the spin-echo could be applied, as described in the next subsection.

Spin echo

If a 180° RF pulse is applied after a certain time interval (TE/2) from the application of the first 90° RF pulse (refocusing pulse), the dephasing created by the effect of the magnetic susceptibility will be canceled out and the normal T2 can be measured. This technique is actually called Spin-echo.
It is crucial to state that the time between the 90° RF pulse and the signal read-out pulse is called TE (echo time). As mentioned, the 180° RF pulse is applied at half of TE. Once the 180° RF pulse has been applied, the spins will rotate by 180° but they will continue their precession in the same direction. Hence, the spins that were precessing faster will be gradually reached by the spins that were precessing slower after the 90° RF pulse. Basically, the more coherent the phases of spins become, the more transverse magnetization will be recovered. In Figure 2.4 different elements of a Spin-echo pulse sequence are presented.

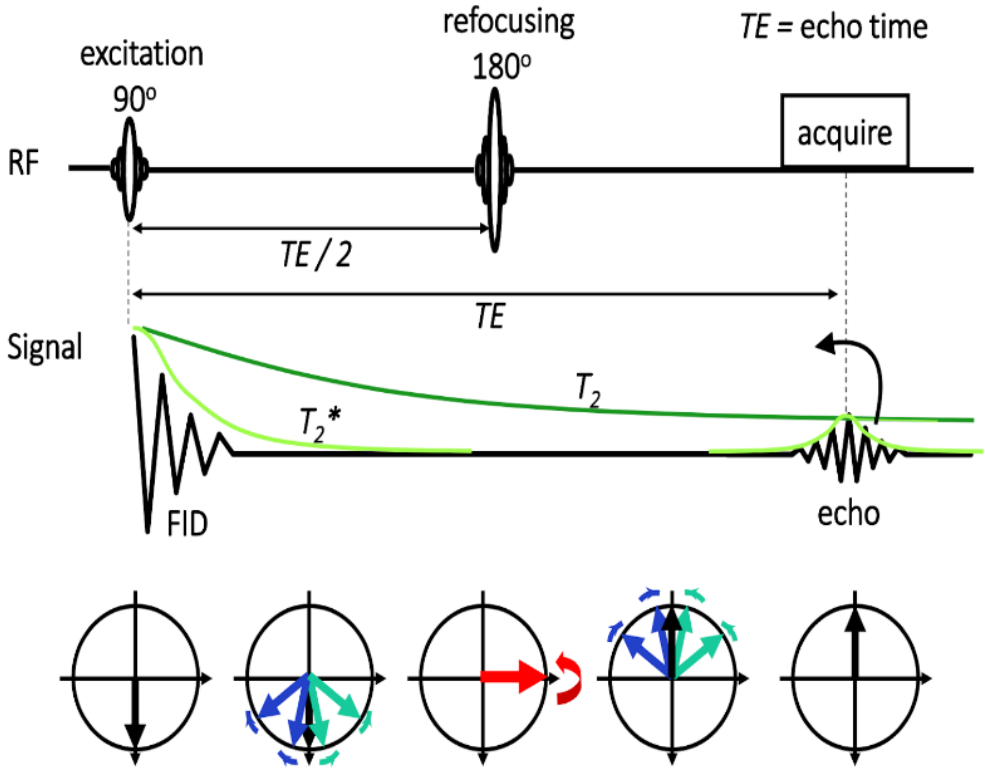

Figure 2.4: Spin-echo pulse sequence. With the application of a 180° RF pulse, it is possible to cancel out the dephasing created by the effect of the magnetic susceptibility. Indeed, after the application of the 180° RF pulse, it is possible to obtain the normal T2, not affected by the magnetic susceptibility.

MR image formation

The principal aim of the use of this type of diagnostic instrumentation is the production of a signal that is giving local information about a specific 3-D object. In order to perform it, two processes need to be considered, which are the selection of the slice and the within-slice localization [18].

Regarding the selection of the slice, the application of a gradient along the z-axis is needed in order to make the precession frequency varying with spatial location. Indeed, as mentioned before, the Larmor frequency is directly proportional to the external magnetic field $\vec{B_0}$. When a gradient is applied, the Larmor frequency of protons in each slice is determined by the following equation:

$$\omega = \gamma(\vec{B_0} + z|\vec{G}z|), \tag{2.6}$$

where $\vec{B_O}$ is the external field, γ is the gyromagnetic ratio of the nucleus of a particle, z is the spatial longitudinal direction and $\vec{G_z}$ is the applied gradient in the longitudinal axis.

By tuning the frequency of the RF pulse, it is possible to decide which slides will be excited.

Taking into account the spatial encoding within the slice, it is essential to combine "frequency encoding" and "phase encoding" in order to perform it.
First of all, it is needed to make the Larmor frequency sensitive to the movement along the x-axis. Thus, in order to obtain this result, a gradient along x needs to be applied. This is defined as frequency encoding:

$$\omega = \gamma|\vec{G}x|x. \tag{2.7}$$

Furthermore, phase encoding is also needed in order to distinguish the points in the brain that have the same x coordinate. The phase encoding, instead, is performed through the application of a gradient along the y-axis for a time duration of τ:

$$\phi = \gamma|\vec{G}y|y\tau. \tag{2.8}$$

It is essential to understand what are the techniques that are used to reconstruct the images. First of all, the definition of the space in which the acquisition of the signal is performed has to be defined. This is called k-space, which contains a specific spatial acquisition strategy.

K-space

The k-space is defined as the extension of the concept of Fourier space, which is well known in MR imaging. This is representing the space covered by the phase and frequency encoding data (ky and kx axes respectively). Once that Fourier transform will be applied, the transformation from the k-space to image space will be achieved, as shown in Figure 2.5.

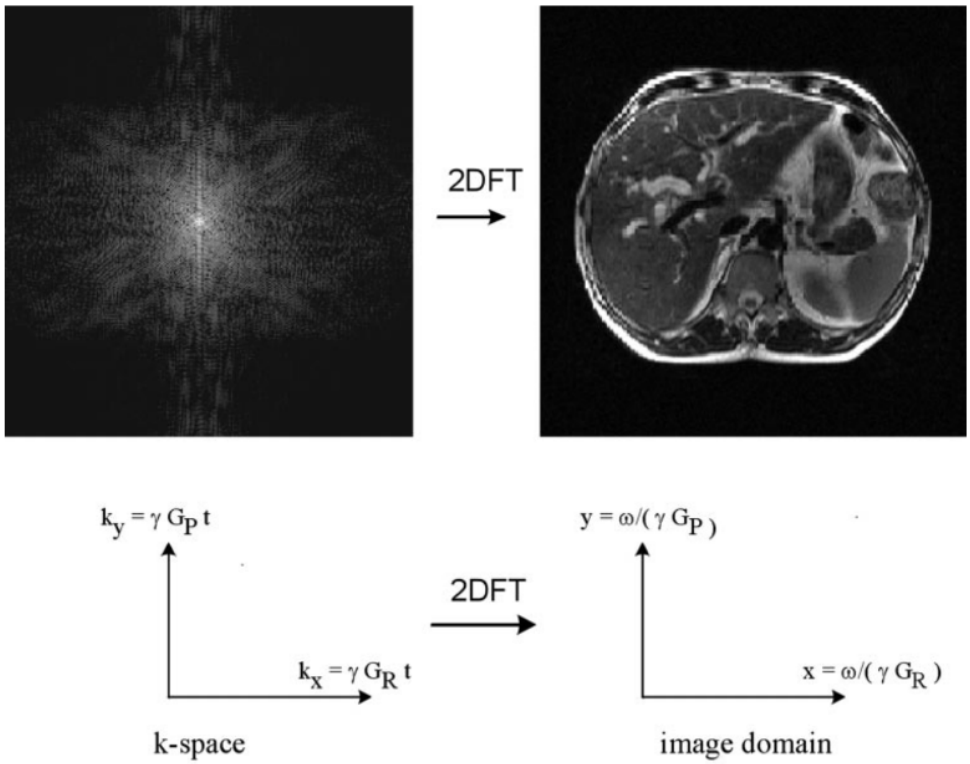

Figure 2.5: Example of the application of the Fourier transform in order to pass from the k-space to the image space. [21]

The Fourier transform is the mathematical tool that is used for this construction process. It is possible to take advantage of the mathematical properties of the Fourier transform in order to decode the k-space representation of the MR signal, S(t), into the magnetization at each spatial location, M(x,y), creating a spatially informative image [22].

Furthermore, from Figure 2.5, it is possible to visualize low and high values, which are associated with low spatial frequencies and high spatial frequencies, respectively. The K-space center, indeed, represents the majority of detected signal, given the fact that the highest values are present in that area.
It is crucial to bear in mind that k-space has an infinite number of points and it is not possible to sample it completely. Indeed, it is needed to discretise the samples in grids or matrices. Several k-space sampling trajectories in MRI acquisition have been proposed, such us the cartesian, radial and twisted projections k-space trajectories.
The cartesian scheme is the most widely used one in clinical scanners. Here, the frequency encoding gradient and phase encoding gradient are separately applied at the signal read-

out, taking into account the interval between RF pulse and read-out pulses. Once the phase encoding gradient for a time τ has been applied, frequency encoding gradient for a time t has been applied and reading out of the signal has been performed at the periodic intervals until the line is filled. Then, the same process is repeated in the next line. The same procedure will be repeated until the sampling designed in k-space is finished.

Echo Planar Imaging (EPI)

Echo-planar Imaging (EPI) was created in 1977 by Sir Peter Mansfield, even before the period of time in which major companies invested in the development of MRI [23]. EPI is working within the application of a rapidly alternating readout gradient (G_x) and within the application of a short phase-encoding gradient that is bursting during transitions (G_y). This results in a train of echoes which is sampling the k-space in a back- and-forth pattern (or zig-zag trajectory). Considering different settings, EPI could be 2-dimensional or 3-dimensional, single or multishot, either applied for spin echo or gradient echo.

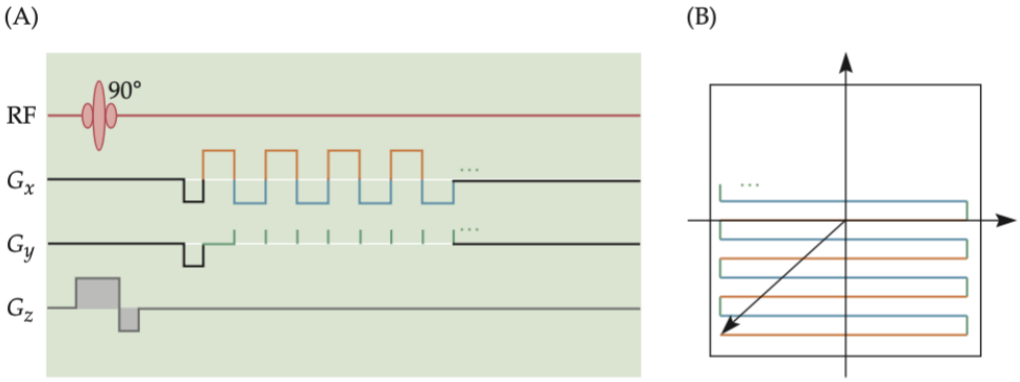

Figure 2.6: An EPI pulse sequence (A) and its k-space trajectory (B). Note that the directions of the gradients are changed rapidly over time to allow the back-and-forth trajectory through k-space. [19]

The required acquisition time for EPI is 0.01-1 seconds per 256×256 single slice image. Thus, the time efficiency of EPI makes it an interesting instrument that is capable of performing acquisitions in an extremely short period of time. Furthermore, it is quite useful for diffusion due to the fact that it makes the images robust to bulk motion.

2.2.2. Encoding Diffusion using MRI instrumentation

One of the most known methods in order to apply the sensitivity of MRI to self-diffusion is the Stejskal and Tanner approach, published in 1965 [24]. The experiment that has been used in this approach is actually the Pulsed Gradient Spin-echo (PGSE). The basic idea of it is shown in Figure 2.7.

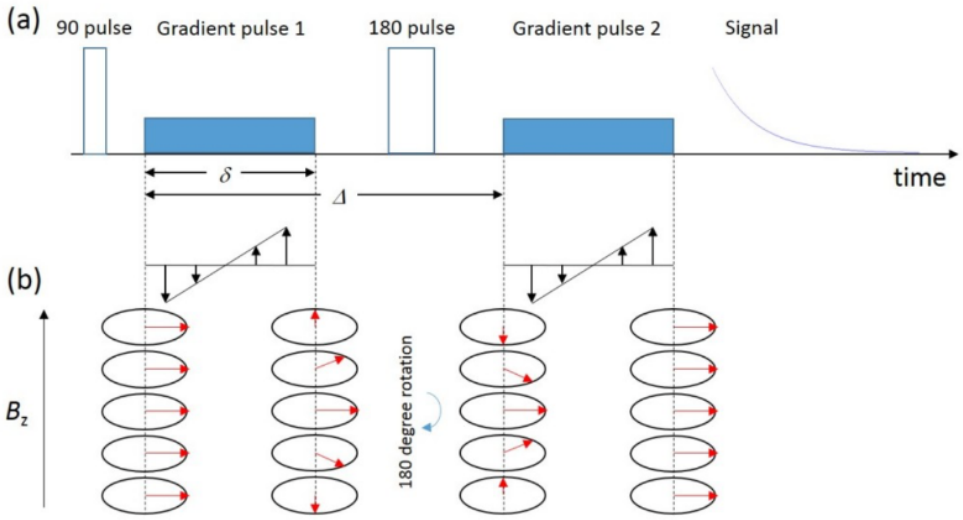

Figure 2.7: Schematic representation of the PGSE pulse sequence. b) Phase evolution of the spins at different locations, related to the application of gradients. It is important to notice that due to the 180° pulse, the phases of the spins are inverted. Hence, the second gradient pulse (which is completely identical to the first one in length and amplitude) serves the purpose of refocusing the phase wrap caused by the first gradient. [25]

In this configuration, the duration of the gradient pulse δ is much shorter than the time in between the two gradients Δ. It is important to consider that the net phase difference (or phase wrap) for the spins between the two gradients is determined by their position at two-time points. Indeed, if the spins are diffusing during the time Δ, the signal will be consequently smaller than the one that could be obtained if the spins stayed in the same position. This is due to the fact that the phase wrap detected in the case of diffusion (movement of the spin) is not null. More crucially, the phase wrap could not be the same for all the spins as it depends on the random motion. Thus, the vector of net magnetization has a smaller module with respect to the hypothetical case in which the spin is not moving.

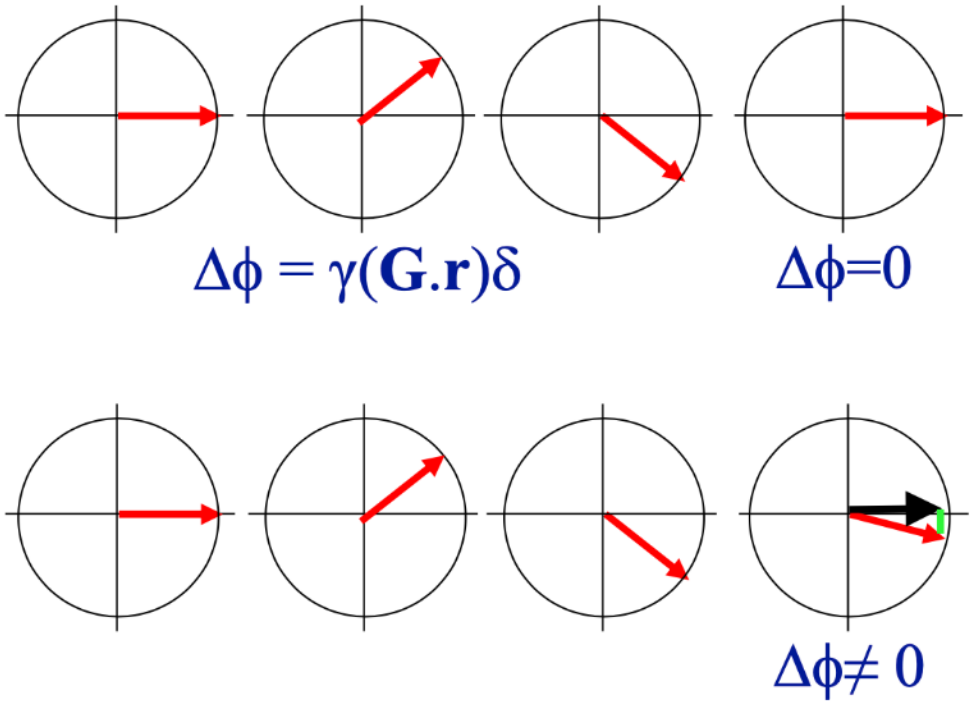

Figure 2.8: Up) Phase evolution of the spins at different locations in the case of no-movement. Down) Phase evolution of the spins at different locations in the case of diffusion movement. Notice that the green line is the projection and the black vector is the net magnetization vector. It is possible to notice that in the case of null phase wrap (no diffusion) the net magnetization is higher than in the other case.

In dMRI, the signal measured by the PGSE sequence can be represented by the following equation:

$$S = S_0 e^{-bADC}, \tag{2.9}$$

where S_0 is the signal that has been acquired without the diffusion weighting gradients and Apparent Diffusion Coefficient (ADC) is the apparent diffusion coefficient. S_0 is related to the proton density, which indicates how many protons are present in the tissue, the echo time TE and the relaxation time T2, as shown in the following formulation:

$$S_0 \simeq p e^{-\frac{TE}{T2}}. \tag{2.10}$$

The sensitivity of MRI to diffusion is characterized by the "b factor", which is also known

as the diffusion weighting factor. This is given by:

$$b = (\gamma G \delta)^2 \cdot (\Delta - \frac{\delta}{3}), \tag{2.11}$$

where δ is the duration of the gradient pulse, Δ is the time interval between the application of the first gradient and the application of the second one, γ is the gyromagnetic constant and G is the amplitude of the applied gradient.

From Equation 2.9 it is possible to notice that if b is increasing, the signal is decreasing. It is important to enlighten the fact that in the Equation 2.9 the ADC is present as well. Indeed, it provides a relatively good tissue contrast when the b value is not too high. Although the real value of ADC depends principally on the direction of the diffusion gradient, considering the case of an anisotropic tissue. Furthermore, if the diffusion values are actually high, the attenuation of the signal is more evident. Within a large attenuation of the signal, a large amount of noise could be detected and, for this reason, the estimate value of ADC could be higher than the actual one, corresponding to that specific diffusion time ($ADCest < ADCtrue$). Therefore, the choice of an optimal b-factor's value is crucial in order to obtain a not too noisy image with a good contrast. To resume, a small b-factor's value could relate poor contrast in the image, while a very large value could massively increase the noise in the image. In order to measure possible alterations of the white matter, the b-value that usually is used is 1000 s/mm^2 [26].
Regarding the models that are used in dMRI,DTI and NODDI are the models that have been previously introduced in this chapter.

2.3. Diffusion Tensor Imaging

One of the most popular and widely used models to describe the primary orientation of white matter axonal pathways in the last 20 years is the DTI model. This model was introduced in 1994 by Peter Basser, shortly after the demonstration that tissue organization affects the diffusion-weighted signal obtained with MRI [25]. DTI describes the distribution of water diffusion in 3D space using a second-order tensor D model. This model has been applied to several neuroscientific studies, such as schizophrenia, multiple sclerosis, autism, aging schizophrenia, migraine and many others [27].

2.3.1. Mathematical descriptions of DTI

Practically, a single 2nd-order D tensor in a 3D space is used by DTI to describe the distribution of water diffusion. It is possible to represent the D tensor by busting a symmetrical covariance matrix, as shown in Equation 2.12:

$$D = \begin{bmatrix} D_{xx} & D_{xy} & D_{xz} \\ D_{yx} & D_{yy} & D_{yz} \\ D_{zx} & D_{zy} & D_{zz} \end{bmatrix} = \begin{bmatrix} \vec{v_1} & \vec{v_2} & \vec{v_3} \end{bmatrix} \begin{bmatrix} \lambda_1 & 0 & 0 \\ 0 & \lambda_2 & 0 \\ 0 & 0 & \lambda_3 \end{bmatrix} \begin{bmatrix} \vec{v_1} & \vec{v_2} & \vec{v_3} \end{bmatrix}^{-1}. \tag{2.12}$$

The diagonal elements (D_{xx}, D_{yy}, D_{zz}) correspond to the diffusion coefficients along the direction of x, y, z axes respectively. The elements that are not in the diagonal correspond to the diffusion covariance in between each pair of axes (D_{xy}, D_{xz}, D_{yz}). It is important to notice that eigenvalues of the tensor D need to always assume positive values and, for this reason, the matrix is symmetric. Hence, the parameters involved in the matrix are 6, instead of 9. Considering the decomposition of the tensor, this could be represented by eigenvalues (λ_1, λ_2, λ_3) and eigenvectors ($\vec{v_1}$, $\vec{v_2}$, $\vec{v_3}$). As shown in Figure 2.9, the tensor D could be adapted to the desired diffusion trajectory that needs to be analyzed. In the case of isotropic unrestricted diffusion, the diffusion pattern is equal for each direction, hence, only one parameter needs to be estimated. In the case of isotropic restricted diffusion, random barriers are present, but no preferential direction is defined. Thus, the knowledge of the coordinates of the considered point and its eigenvalues need to be considered to solve the system of equations (3 parameters). In the case of isotropic restricted diffusion, a preferential direction is defined. Thus, 6 parameters are needed to solve the system of equations (D_{xx}, D_{yy}, D_{zz}, D_{xy}, D_{xz}, D_{yz}).

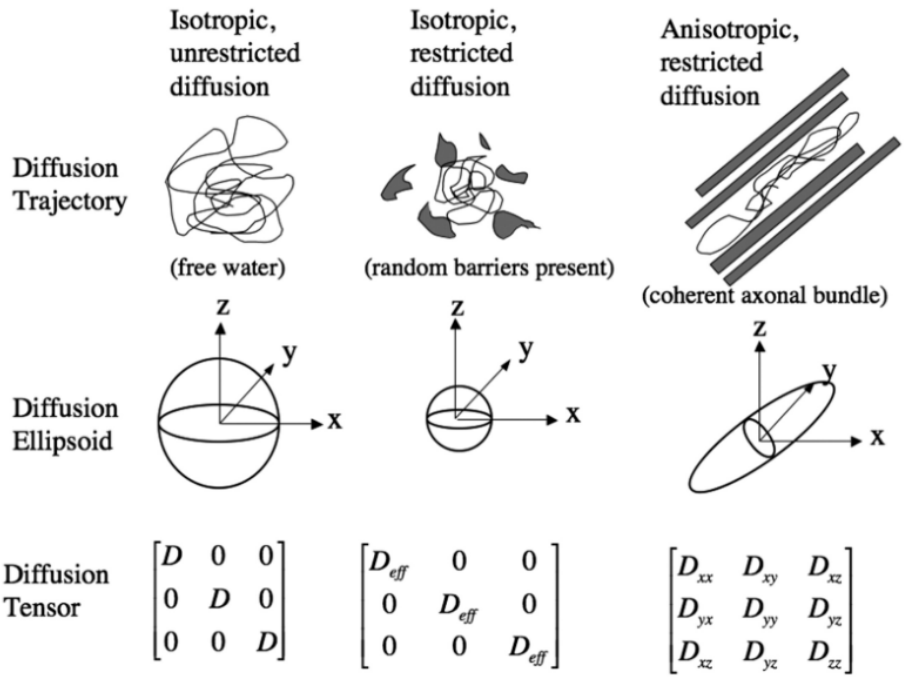

Figure 2.9: Diffusion ellipsoids and tensors for isotropic unrestricted diffusion (right), isotropic restricted diffusion (center), and anisotropic restricted diffusion (left). [28]

2.3.2. Tensor fitting

The tensor D is estimated for each voxel by fitting a tensor into the diffusion attenuated MRI signal within the use of a linear/non-linear least square fitting. As mentioned before, only 6 elements are required for the estimation. Hence, with a minimum acquisition of 6 Diffusion Weighted Imaging (DWI) volumes, it is possible to compute a tensor D for all the voxels that are composing the image. FMRIB Software Library (FSL) could be one of the softwares available that can be used to perform the tensor fitting.

2.3.3. Computing DTI metrics

Taking into account the 3 eigenvalues, several additional rotationally invariant diffusion metrics are commonly used for the microstructure description of a particular voxel [28]. One of them is the Mean Diffusivity (MD), which represents the mean of the 3 eigenvalues and describes the directionally averaged diffusivity of water within a voxel:

$$MD = \frac{\lambda_1 + \lambda_2 + \lambda_3}{3} = \frac{Tr(D^{eff})}{3}, \tag{2.13}$$

where $Tr(D^{eff})$ is the trace of D, which is the sum of the 3 eigenvalues and represents another measure of orientationally averaged diffusion [28].
It is also essential to consider the Axial Diffusivity (AD) and Radial Diffusivity (RD), which are defined with the following equations:

$$AD = \lambda_1; \tag{2.14}$$

$$RD = \frac{\lambda_2 + \lambda_3}{2}. \tag{2.15}$$

.

AD is represented by the primary longitudinal eigenvector λ_1, which is reflecting the organization of the parallel axons. The RD is the average of secondary and tertiary eigenvectors, which are reflecting the myelination process present in the axons [29].

The other 2 important metrics that need to be taken into account are Fractional Anisotropy (FA) and Relative Anisotropy (RA). These indicate the degree of directionality of intravoxel diffusivity and are expressed by the following equations:

$$FA = \frac{\sqrt{(\lambda_1 - \lambda_2)^2 + (\lambda_2 - \lambda_3)^2 + (\lambda_3 - \lambda_1)^2}}{\sqrt{2}\sqrt{(\lambda_1)^2 + (\lambda_2)^2 + (\lambda_3)^2}}; \tag{2.16}$$

$$RA = \frac{\sqrt{(\lambda_1 - \lambda_2)^2 + (\lambda_2 - \lambda_3)^2 + (\lambda_3 - \lambda_1)^2}}{\lambda_1 + \lambda_2 + \lambda_3}. \tag{2.17}$$

Practically, these values are indicating the level of homogeneity of the fiber orientation. Indeed, taking the example of FA, if the homogeneity is high, the value of FA will be low (assuming a spherical shape). If the homogeneity is low, the value of FA will be higher (assuming an elliptic shape). The considered range for FA goes from 0 to 1 and this is often related to the tract integrity of the white matter. All the parameters are represented in Figure 2.10.

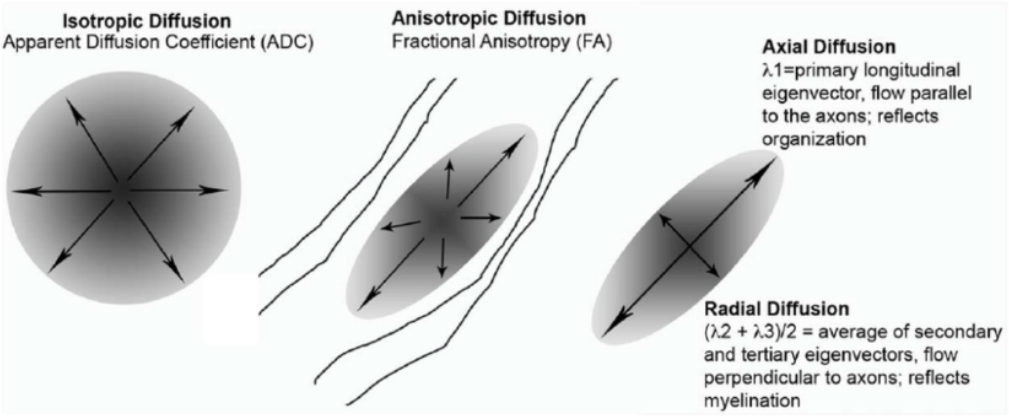

Figure 2.10: Graphical representation of ADC, FA, AD and RD. [30]

2.4. Neurite orientation dispersion and density imaging (NODDI)

2.4.1. Mathematical descriptions of NODDI

The aim of NODDI is the description of the water diffusion in each voxel considering three compartments, including intra-neurite, extra-neurite and free-water compartments. Mathematically, it is possible to define the diffusion weighted MR signal as a linear combination of the signals related to these three compartments:

$$S = [1 - f_{iso}][f_{ic}S_{ic} + (1 - f_{ic})S_{ec}] + f_{iso}S_{iso}, \tag{2.18}$$

where:

- S is the normalized diffusion weighted signal;
- S_{ic}, S_{ec} and S_{iso} are the normalized diffusion weighted signal decays contributed separately by the intra-neurite compartment, extra-neurite compartment and free water compartment;
- f_{ic} and f_{iso} are the volume fractions of the respective compartments.

Intracellular model

In particular, S_{ic} (which is representing the normalized signal contributed by the intra-neurite compartment) could be described by the following equation:

$$\ln S_{ic} = \int_{\mathbb{S}^2} f(\vec{n}) e^{-bd_{||}(\vec{q}\times\vec{n})} d(\vec{n}), \tag{2.19}$$

where $f(\vec{n})$ is the probability density of a stick (defined as a cylinder with a null radius) along the direction $\vec{n}$, $\vec{q}$ is the diffusion-weighted gradient direction and $d_{||}$ represents the intrinsic diffusivity.
In this case, the Watson distribution has been used as the mathematical description of $f(\vec{n})$, which is defined by the concentration parameter κ and by the mean orientation $\vec{\mu}$. A graphical example of Watson distribution has been reported in Figure 2.11.

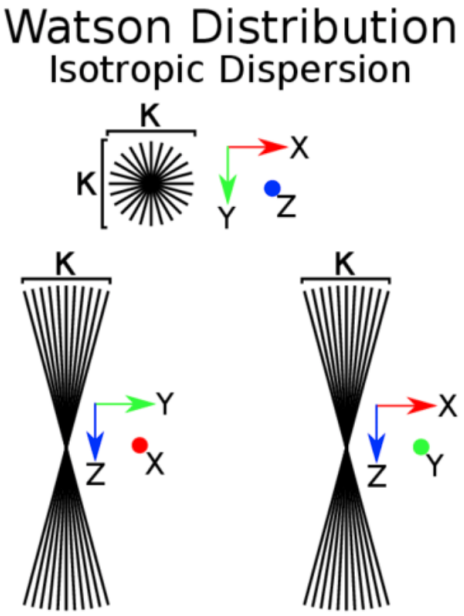

Figure 2.11: Schematic representations of Watson distributions. Watson models isotropic dispersion defined by the concentration parameter κ and centered around direction μ. Figure taken from [31], Fig 4.2.

It is crucial to state how the water is moving along the intracellular compartment. The motion here occurs freely along the direction of axons and dendrites but is massively restricted in the perpendicular direction of the axons, due to the presence of the membrane barriers. This explains why the motion in the intracellular compartment can be associated with the restricted diffusion.

Extracellular model

Regarding the second term S_{ec}, this represents the normalized signal which is related to the extra-neurite compartment. This compartment represents the glial cells and cell bodies, which are modeled as a cylindrically symmetric tensor (known as zeppelin). The formulation of the term S_{ec} can be described by the following equation.

$$\ln S_{ec} = -b(\vec{q})^T \left(\int_{S^2} f(\vec{n}) D(\vec{n}) d\vec{n} \right) \vec{q}, \tag{2.20}$$

where $D(\vec{n})$ is an anisotropic tensor with the same eigenvalue in the two perpendicular directions. $\vec{n}$ is defined as the principal direction of diffusion. It is also important to clarify some aspects inherent to the diffusion coefficient D. Indeed, if the diffusion is defined along a parallel direction with respect to the direction of the vector $\vec{n}$, then the diffusion coefficient associated with it is defined as $d_{||}$. If the direction of diffusion is parallel to the vector $\vec{n}$, then the considered diffusion coefficient is d. The aforementioned $d_{||}$ and d need to be modified according to the Watson distribution in the extracellular compartment. Moreover, it is important to remember that the apparent diffusion coefficients need to be defined.

Indeed the parallel and perpendicular apparent diffusion coefficients for the extracellular compartment are defined as follows:

$$d'_{||} = d_{||} - d_{||} f_{ic}(1 - \tau_1);$$
$$d'_{\perp} = d_{||} - d_{||} f_{ic} \left(\frac{1 + \tau_1}{2} \right).$$

The term τ_1 indicates the effect of orientation dispersion on the apparent diffusivities. This has been defined by Abramowitz and Stegun [32, 33] as follows:

in which F is a function defined as $F(x) = \frac{1}{2}\sqrt{\pi} e^{-x^2} erfi(x)$, where $erfi$ is the imaginary error function (sigmoid function that occurs often in probability, statistics, and partial differential equations). The value of τ_1 is varying between $\frac{1}{3}$ for isotropically-dispersed orientations (thus when κ is 0) and 1 for strictly parallel orientations (κ tends to infinity). In the extracellular compartment, the movement of the water is restricted by the glial cells and the cell bodies. Indeed, the diffusion of the water is hindered by these two types of cells and, for this reason, the diffusion here is referred to as hindered diffusion.

CSF compartment

Taking into account the last term S_{iso}, this represents the normalized signal coming from the free water compartment (modeled as a ball) and it is defined as:

$$\ln S_{iso} = -bd_{iso}, \tag{2.21}$$

where d_{iso} is the free water diffusivity, which is referred to as isotropic diffusion. Indeed in the CSF compartment the water molecules are free to move and there isn't the presence of a preferential direction of movement.

In general, NODDI provides the estimation of three key aspects related to the neural tissue at each voxel, which are Neurite density index (NDI), Orientation dispersion index (ODI) and the Free water fraction (FWF). The Neurite density index quantifies the packing of density of axons or dendrites. Thus, the more axons there are, the higher is the NDI value. The Free water fraction estimates the extent of the contamination caused by the CSF. Thus, this is defined as the volume fraction of free water within that volume, or precisely, it is the FW (free-water) volume divided by voxel volume [34]. The Orientation dispersion index, instead, describes the degree of dispersion of the dendrites. It could assume a value between 0 and 1 (0 for strictly parallel dendrites and 1 for fully dispersed dendrites). Furthermore, it could be mathematically described by the following formulation derived from the Watson distribution:

$$ODI = \frac{2}{\pi} arctan(\frac{1}{\kappa}). \tag{2.22}$$

.

In Figure 2.12, the key aspects related to NODDI are presented and compared with techniques such as DTI and DKI. It is possible to state that these techniques can provide a composite view of the neural tissue, but it is not possible to show what influence the singular tissues have in the final image. Within NODDI it is possible to perform this type of analysis.

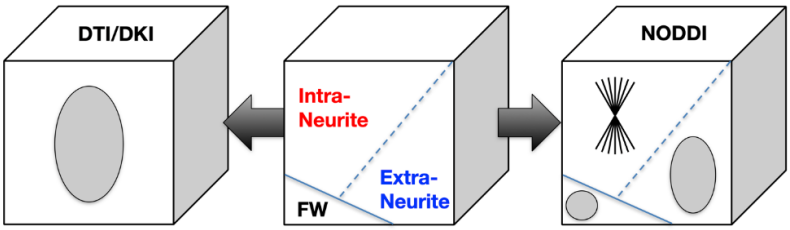

Figure 2.12: Diagram representing the difference between DTI/DKI and NODDI. DTI/DKI can only provide a composite view of the complex neural tissue, while NODDI can offer alternatives that could enable the investigation of the contribution given by the singular tissue components. [35]

2.4.2. Model fitting for NODDI

The model is based on the search for a set of parameters $\vec{p}$ that maximize the logarithm of the likelihood between the performed measure and the predicted signal for each voxel. The logarithm of the likelihood is defined by the following formulation:

$$logL(\vec{p}) = -2Mlogv + \sum_{m=1}^{M} logI_0\left(\frac{S_m S'_m(\vec{p})}{v^2}\right) + logS_m - \frac{S_m^2 + S'_m(\vec{p})}{2v^2}. \tag{2.23}$$

.

In this equation, S_m represents the performed $m-th$ measure, while S'_m is the predicted signal from the NODDI model at the corresponding acquisition. v is the spread of rician distribution (which is the distribution that has been used in this model fitting) and I_0 is a Bessel function of the first kind (in which the 0 indicates that a 0-order Bessel function has been used).
The aforementioned fitting procedure is based on two stages. In the first stage, a grid search is used before the gradient descent search in order to identify a set of plausible parameters in the range of the microstructure for each voxel. This set will consequently be used as the input for the second stage for the procedure. The second stage consists of the gradient descent search. NODDI fitting has been carried out with the matlab package described in *http://mig.cs.ucl.ac.uk/index.php?n=Tutorial.NODDImatlab* [35].

2.4.3. NODDI metrics

The following parameters have been included to the complete set of model in NODDI:

- f_{ic}, the volume fraction of the intracellular compartment, which is referred to the NDI values;
- f_{iso}, the volume fraction of the free water compartment, which is related to the FWF values;
- κ, the concentration parameter of the Watson distribution, which is used to calculate the value of ODI applying the Equation 2.22;
- $\vec{\mu}$, the main orientation of the Watson distribution;
- $d_{||}$, the intrinsic diffusivity;
- d_{iso}, the isotropic diffusivity of free water.

It is important to state that the values of the intrinsic and isotropic diffusivity that have been used, are the ones that are reported by Zhang et al. [32], which are $d_{||} = 1.7 * 10^{-3} mm^2/s$ and $d_{iso} = 3.0 * 10^{-3} mm^2/s$.

2.5. Comparison between DTI and NODDI

In this section, the differences between DTI and NODDI have been analyzed in order to explain what are the theoretical concepts that support the utility of NODDI compared to DTI.
Generally, it is crucial to define what is the purpose of the microstructural imaging in biomedicine. The aim is related to the production of quantitative imaging biomarkers that reflect the properties of interest inherent to the tissues. As mentioned before, DTI has been described as a useful tool in order to perfectly achieve these purposes. Although, a single tensor model in DTI assumes a single Gaussian distribution for the water diffusion and, for this reason, it could be considered as too simple. Indeed, in Jones et.,al [36], it has been stated that the provided results from DTI have been given implausible interpretations quite often. This is related to the fact that there is a lack of specificity with respect to the properties of tissue microstructure. Going deeper into the characteristic parameters that the DTI is offering, it is needed to state that the values of FA, MD, and RA should be related to common conditions. For instance, it has been stated that myelin loss and cell death conditions are indicated by an increase in the MD values and a decrease in the FA values. Even if they are two different conditions, they are pointed by the same behavior in terms of these two values. This effect is shown in Figure 2.13, reported below.

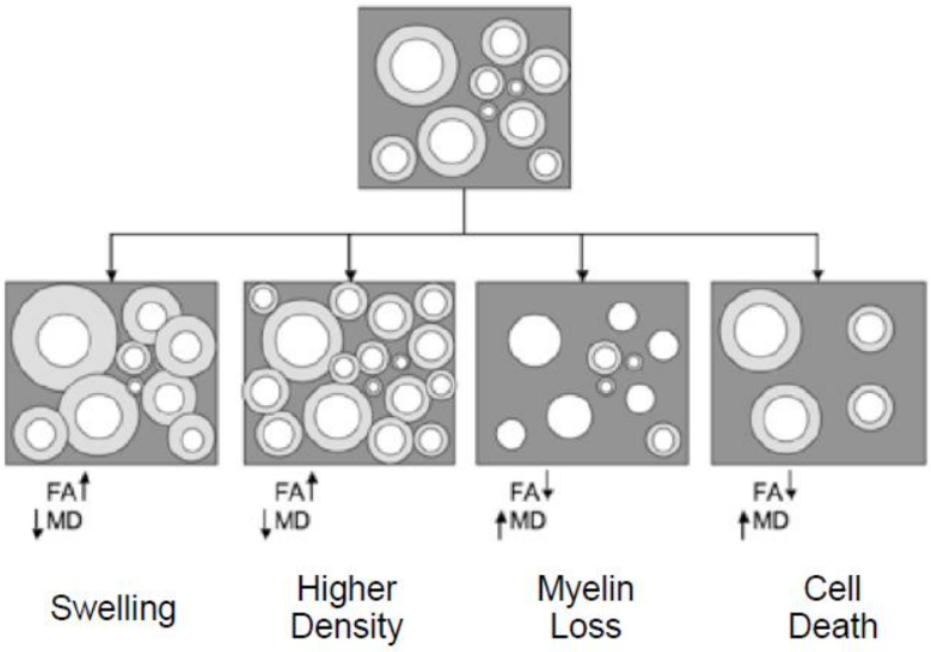

Figure 2.13: Illustration of the FA and MD values under multiple conditions: Swelling, Higher Density, Myelin Loss, and Cell Death. It is crucial to notice that the FA and MD behavior related to Myelin Loss and Cell Death is identical. The same can be stated for Swelling and Higher Density conditions.

Furthermore, FA could be affected by several factors, such as permeability of axonal membranes, myelination, axonal orientation dispersion, and many others. NODDI, instead, has been considered by Ai Wern Chung et., al [37] as a promising model for the estimation of multiple diffusion compartments from MRI data acquired, within the requirement of a clinically feasible time. Moreover, in terms of reproducibility, it has been reported that NODDI measurements are varying more than the measures that DTI is offering. This could be caused by the fact that NODDI is more susceptible to noisier parameter estimates. Thus, it may have greater sensitivity to subject heterogeneity [37].

2.6. Image Analysis for Diffusion MRI

Diffusion MR Image Analysis is the next step that, according to the diffusion MRI (dMRI) processing pipeline, it is performed immediately after the estimation of the dMRI metric. The most common approaches that have been used in human white matter applications include Voxel-Based Analysis (VBA), ROI analysis and tract-based spatial statistics

(TBSS). In this chapter, these approaches are going to be introduced with the purpose of clarifying each step involved in the MRI processing pipeline.

2.6.1. Voxel-based analysis (VBA)

The aim of VBA is to perform correlation analysis voxel by voxel and, a whole-brain white matter VBA. However, it is essential to bear in mind that VBA in diffusion MRI can be a limited technique due to the choice of kernel width for spatial smoothing and the good alignments of brain structures by spatial registration [38]. Indeed, a precise spatial registration could be used in order to perform an accurate alignment of the thin structures and avoid topological variabilities. Although, it is essential to bear in mind that this kind of spatial registration is not often representing reality. Furthermore, in order to improve the sensitivity to abnormalities and to reduce the effects of misalignments, it could be suggested to smooth with an appropriate value of kernel width. Although, the choice of this parameter is often arbitrary, and, for this reason, depending on this value it is possible to obtain results that are extremely different from each other. Indeed, Hae-Jeong Park et al [39] have stated that the smoothing kernel size should be small enough to detect smaller structures but large enough to resist possible errors. It is also important to mention that the choice of the smoothing kernel size should potentially increase the partial volume effect in the images, especially in the voxels that are located in between tissues of different types.

2.6.2. Tract-based spatial statistics (TBSS)

Tract-based spatial statistics (TBSS) is a fully automated voxel-wise approach that deals with the aforementioned issues related to the VBA analysis [40]. Indeed, this approach can overcome the alignment problems by working in the space of individual subjects' tractography results, and, most importantly, it doesn't require pre-smoothing. White matter skeleton is limiting all the TBSS statistical analyses. The skeleton is identified by the search for the center of all white matter fiber bundles that are common across the subjects involved in the specific study [40].

2.6.3. ROI analysis

ROI analysis is based on grouping the anatomically related voxels within the same anatomical unit. This process can effectively improve statistical power as it strongly decreases the number of multiple comparisons [41]. However, it is known that this type of analysis is not suitable for a whole-brain analysis and it can have problems related to reproducibility

[41]. ROIs could be defined in several ways: manual delineation, using tractography, using white matter atlas, and many more. It has been stated that the manual delineation of ROIs could depend on the ability and the experience of the scientist that is performing the analysis. Indeed, White matter atlases are used to overcome these types of issues. These are often created by experts with a well-defined neuroanatomy background and, hence, this could theoretically minimize the lack of knowledge of the ones that are performing the study.

3 | Alteration of the white matter in migraine patients: An overview

3.1. White matter in the human brain

White matter in the human brain includes the fiber tracts that are connecting cortical and subcortical brain areas. They are composed mainly of glial cells and axons that could be myelinated or not-myelinated.

3.1.1. White matter microstructure

The main components that are included in a voxel of white matter microstructure are axons, intra-axonal space, myelin, extracellular space, glial cells, and vascular systems. In Figure 3.1 all these components are listed, showing the respecting illustrations.

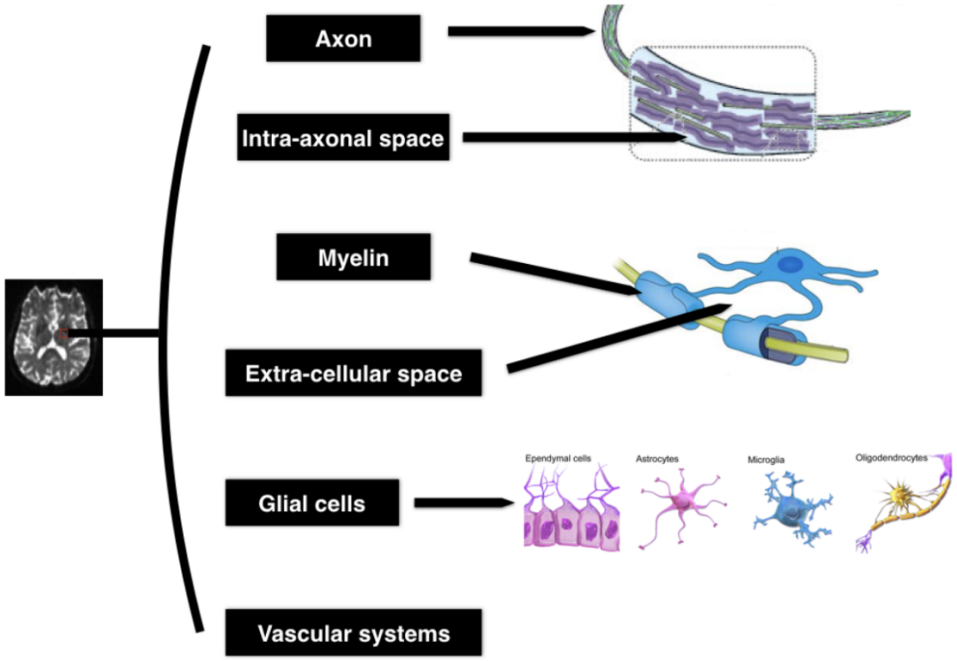

Figure 3.1: Illustration of all the components that are present in a voxel of human white matter according to an MR imaging point of view. [15]

Glial cells

Glial cells are defined as the non-neuronal cells present in our brain and nervous system. A variety of subtypes of glial cells have been already discovered, such as oligodendrocytes, microglia, and astrocytes. It is important to bear in mind that each subtype is specialized for a particular function [42]. The glial cells are not able to start an action potential and, for this reason, in the past, they have been considered housekeepers that ensure the functionality of the neurons. Recently, it has been discovered that this is not completely true. Indeed, the astrocytes, for instance, are considered to be the key components of the synapses because of the fact that they can influence information process modality [42]. In Figure 3.2, the principal glial cells are represented.

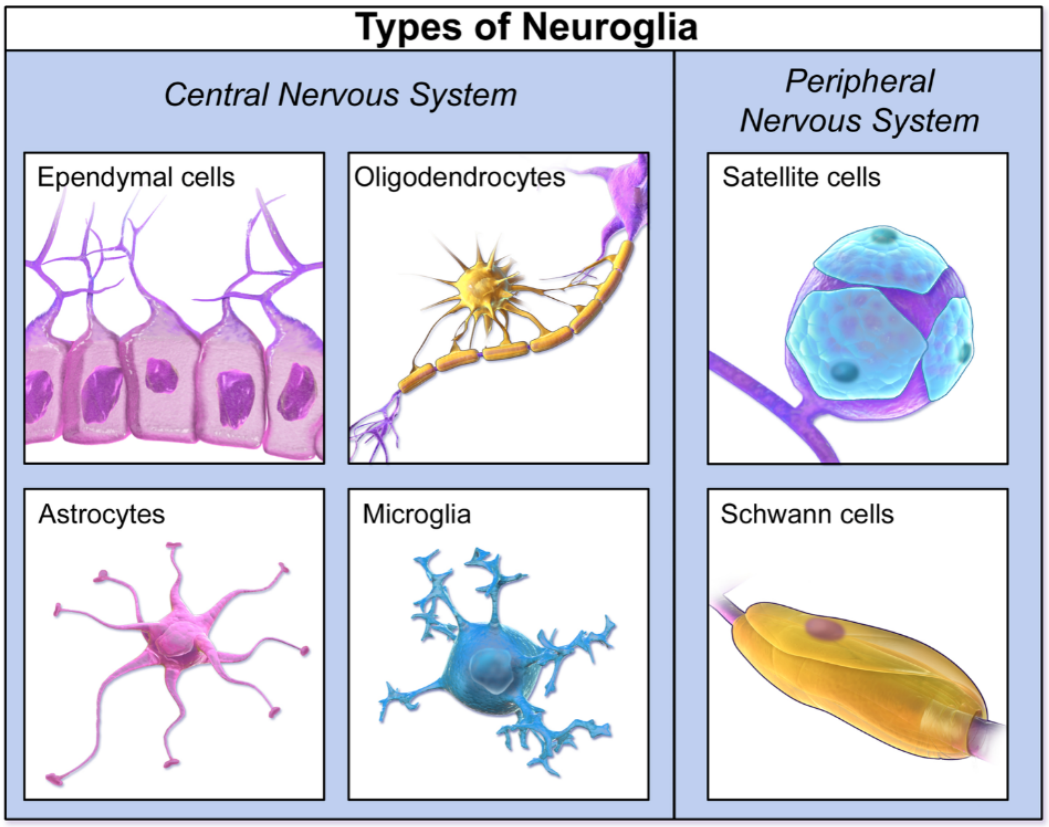

Figure 3.2: Major types of glial cells present in the Central Nervous System and in the Peripheral Nervous System. [43]

Regarding the microglia, these are the brain's immune cells, used in case of protection against injuries or diseases. Microglia are identifying anomalous events and they are recruited to initiate a response that removes the toxic agent or clears away the dead cells. Practically they can be considered the brain's protectors [43].
Taking into account the macroglia, this includes astrocytes, oligodendrocytes, and the aforementioned cells in the Peripheral Nervous System (Schwann cells and satellite cells). The astrocytes are star-shaped cells that maintain the functionality of the neuron. Indeed, they are responsible for the control of the levels of neurotransmitters around the synapses within the provision of metabolic support and the control of important ions like potassium. The oligodendrocytes, instead, provide support to the Central Nervous System's axons, in particular to those that travel long distances within the brain. Hence, they are responsible for the production of the myelin, which is wrapped around the axons and works as a layer of insulation. Furthermore, the myelin sheath allows electrical messages to travel faster through the Ranvier Nodes. Actually, myelin is the substance that gives white matter its name, because of the color that the sheaths assume. Regarding the Schwann cells,

these are cells that are similar to the oligodendrocytes. Hence, they are responsible for the myelination of the Peripheral Nervous System's neurons. Finally, the Satellite cells are the ones that surround the neurons in the sensory, sympathetic, and parasympathetic ganglia and assist in the regulation of the chemical environment [43].

Myelin

The myelin sheath is defined as the protective coating surrounding the nerve fibers, similar to the protective insulation around electrical wires. This coat is enabling the electrical pulses between nerve cells to travel back and forth at higher velocity [44]. The sheath has a thickness of about 10 nm and it is formed by 80% of lipids and 20% of proteins. The segments of myelinated axons are repeated for each 12 nm of length and the gaps between those segments are called Nodes of Ranvier. Due to the saltatory conduction, the individual myelin sheaths are the ones that are causing the leap of the signal from one node of Ranvier to the next [45]. It is crucial to take into account the fact that myelin sheaths are not the ones responsible for the start of the action potentials per sé. Instead, the electrical wave created at each node propels the action potential to the end of the nerve, where it can be transferred to the next neuron. This mode of propagation of the signal saves energy, due to the fact that the use of the sodium/potassium pumps is not needed under the myelin sheath [45].

Axons

The axon should be seen as a cable with a diameter that can be considered thinner than a human hair, in which the electrical impulses are traveling from one neuron to another [43]. The axon diameter should be considered one important axonal feature. The relationship between the signal transmitting speed and the diameter should be considered linear. Therefore, the larger the axon diameter, the faster the propagation of the signal. In the human brain, the considered range of the axon diameter is going from 0.1 um to 10 um. It is also important to state that there are variations in axon diameter even within the same tract. Another important axonal feature is axon density. Neurodegenerative diseases and aging could cause a decrease in axon density. Furthermore, the spatial organization of the axons could potentially indicate the presence of neurological diseases.

The intra-axonal space

The intra-axonal space is the one formed by the axon's membrane and it contains macromolecules, proteins, mitochondria, filaments, and microtubules. The filaments have the

purpose of preserving the shape and the internal organization of the axons. Regarding the microtubules, these are the structures that support the material transportation from the body of the cell to the axon terminals.

The Extracellular space

The term extra/cellular space is indicating all the space outside the cell membrane. The issue related to this space is the measurement of its volume. Until now, it was not possible to find an accurate way of measuring this volume. In Eva Sykova et,.al [46], the registered fraction of this space resulted in 15-35% in the non-human adult brain. In order to perform this type of measurement, an invasive microscopy technique has been applied.

Vascular system

The microvascular architecture of the human white matter could be considered extremely complex [47]. Indeed, it is possible to find complex fountain-like rami of arteries, veins and capillaries. In the microvasculature, it is possible to state the presence of microscopic motions of water, including molecular diffusion and microcirculation of blood in the capillary network [48]. This effect is faster than the aforementioned water diffusion and, for this reason, it could be difficult to measure.

3.1.2. White matter tracts

The white matter tracts could be broadly classified into 3 groups, according to their connectivity, origins, and terminals. These groups are called projection fibers, association fibers, and commissural fibers [49].
Regarding the projection fibers, these are the ones that connect the cortical areas with the deep gray nuclei, cerebellum, spinal cord, and brainstem or vice versa. With the use of DTI, it is possible to identify fibers such as corticospinal fibers, corticobulbar fibers, geniculocalcarine fibers, and plenty more.
The association fibers, instead, connect different cortical areas within the same hemisphere. These types of fibers can be classified as long-range or short-range. The principal long tracts include cingulum, Superior Longitudinal Fasciculus (SLF), superior and inferior occipito-frontal fasciculus, uncinate fasciculus and inferior longitudinal fasciculus.
Taking into account the commissural fibers, these connect similar cortical areas in the two hemispheres, including the corpus callosum and the anterior commissure [49].

3.2. Migraine overview

Migraine has been known as a pathological condition that afflicts humankind since antiquity. This could be classified as an intense pulsatile painful neurological condition [3]. Furthermore, migraine is ranked by the World Health Organization (WHO) as 19th among causes of years lived with disability [50]. According to the International Headache Society, the headache caused by migraine is defined as pulsating and it lasts for 4/72 hours, accompanied by nausea and vomiting as well [51]. The entire migraine experience is still not easy to define in terms of perceptions, emotions, and inner troubles that the patients are suffering [52]. Hence, it is often difficult for a person affected by migraine to clearly explain the discomfort that the headache can cause. Although health care professionals developed some clinical criteria to guide diagnoses and subsequent treatment. Indeed, the characteristics of migraine without aura have been listed in the second edition of the International Classification of Headache Disorders (ICHD-2) [53] and these are:

- recurrent headaches, minimum 5-lifetime attacks;
- unilateral, pulsating, moderate, or severe intensity pain;
- untreated or unsuccessfully treated headache duration of 4 to 72 hours;
- at least one of the following conditions: photophobia, phonophobia, or nausea caused by the migraine attack.

These symptoms could be different depending on the migraine attack phase that we are considering [54]. Indeed, Migraine attacks should present different phases, which are:

- Prodrome;
- Aura;
- Headache;
- Postdrome.

The Prodrome could be considered the start of the migraine attack, and it could last from few hours to several days on some occasions [54]. Most migraine patients will experience this phase, but not necessarily before every migraine attack. With the administration of medications, mindfulness meditation practice, relaxation therapy, minimization of other trigger factors (such as alcohol), or other biobehavioral techniques applied during Prodrome, in some cases, it is possible to prevent the headache attack entirely. The typical symptoms that Prodrome can cause are changes in mood, fatigue, sensitivity to light and sound, nausea, insomnia, muscle stiffness, constipation, and many more.

Talking about the aura, this is a phase that does not necessarily occur during every migraine attack, as well as many other mentioned phases. Aura could affect the patient for a time interval of 5 to 60 minutes. The typical symptoms caused by this phase are vision loss or blurry vision, the appearance of geometric patterns, blind spots in one or both eyes, shimmering or flashing lights, etc [54]. This phase can serve as another warning of a potential headache since it typically precedes the headache phase. Even though not all auras are followed by headaches.

Regarding the proper headache phase, this can last from 4 hours to up to three days, and it's characterized by pain on one or both sides of the head. Other symptoms should be included in this phase, besides the pain. Indeed, the headache phase can also cause an inability to sleep, anxiety, nausea, and sensitivity to light, smell, and sounds.

Postdrome is the phase that occurs after the end of the headache phase. This phase occurs in almost 80% of migraineurs. Postdrome should be also called the "migraine hangover" and it usually lasts from 24 to 48 hours. [54] The typical symptoms that this phase could cause are body aches, trouble concentrating, sensitivity to light, dizziness, and fatigue.
In Figure 3.3, it is possible to visualize all the different phases of a migraine attack, considering the severity associated with each one of them.

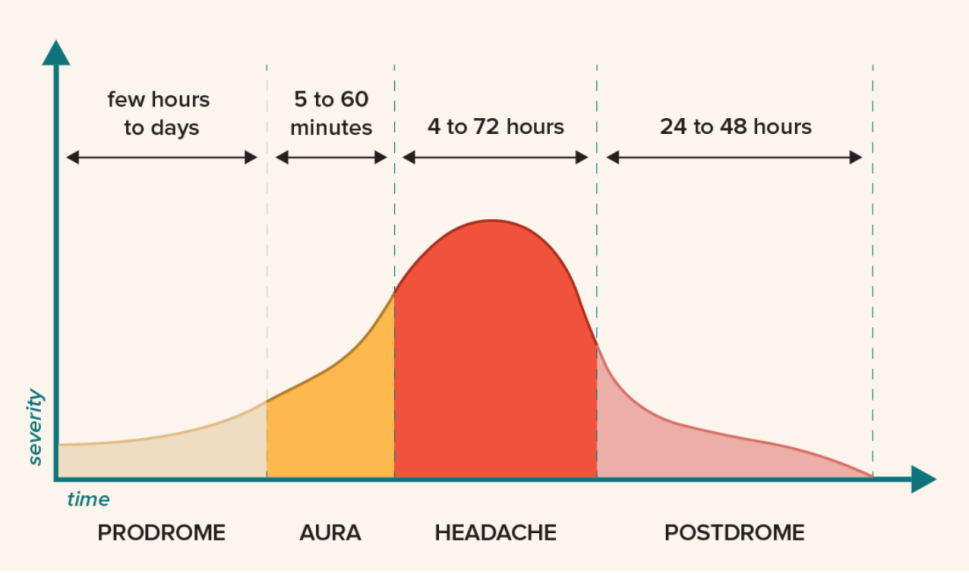

Figure 3.3: Illustration of the severity of the different phases of a migraine attack displayed as a function of time. In order, the four phases are: Prodrome, Aura, Headache, Postdrome. [55]

Besides different phases, it is crucial to state the fact that there exist different types of migraine conditions, classified according to the intensity and duration of the symptoms. Therefore, principally two types of migraines have been identified, which are episodic and chronic migraine. In sections 3.2.1 and 3.2.2, the features related to episodic and chronic migraine have been clearly identified, enlightening the consistent differences that these two conditions are expressing.

3.2.1. Episodic migraine

EM is characterized by several headache attacks, in particular not more than 14 headaches per month over a span of three months [56]. As mentioned before, not all headaches are caused by migraine. Thus, it is highly suggested to classify the symptoms in a schematic and accurate way.

Menstrual Migraine

MM could be considered as a particular type of EM, depending on the strength and duration of the symptoms.
Generally, MM refers to migraine attacks that are related to menstruation. These attacks occur during the menstrual period. It has been stated that half of women with migraine report menstruation as a trigger for their migraine attacks [57]. These attacks tend to be more severe and less responsive to general treatments.
It is possible to distinguish two types of MM [4]:

1. Migraine related to menstruation (MRM), in the case in which migraine attacks are present at other times of the month, and not only during menstruation;
2. Pure Menstrual Migraine (PMM), in the case in which migraine attacks are present only during menstruation.

The cause of this phenomenon could be due to the link between migraine and falling levels of the hormone oestrogen [57]. Indeed, it's the natural drop in oestrogen levels that is strictly linked to menstrual migraine. This drop is usually present before the starting of the menstruation. Furthermore, another factor that could be linked to MM is the level of prostaglandin [58]. Especially in women who have painful and heavy periods, the levels of this hormone could be high and this could also play a role in MM.

3.2.2. Chronic migraine

CM has been defined by the revised International Classification of Headache Disorders (ICHD-2) as headaches in 15 or more days per month, for a span of three months. In this case, it is defined as chronic when the experienced symptoms for 8 or more days meet the criteria for migraine without aura and/or respond to migraine-specific treatment, occurring in a patient that had already experienced at least five prior migraine attacks not attributed to medication overuse and other causative disorders [53]. Due to the enormous number of attacks per month, CM is considered extremely disabling and it can have a large impact on the daily life of the subject. Indeed, this condition has been linked to higher unemployment and disability, due to the frequent inability to work experienced by this type of sufferers. It has been stated that CM could have a higher incidence when the patient is presenting psychological illness, such as anxiety, depression, chronic pain, or cardio-respiratory issues [56].

3.2.3. Relationship between Episodic Migraine and Chronic Migraine

Due to the massive research work that has been performed, a connection between EM and CM has been found, although the relationship between the two types of migraine is complex to define. The most important observational studies that have reported useful information inherent to the distinction between EM and CM are, for instance, the International Burden of Migraine Study (IBMS) [59], the American Migraine Prevalence and Prevention (AMPP) study [60], and the German Headache Consortium (GHC) study [61]. As a result, it has been stated that EM could progress to CM at the rate of 2.5% per year. Furthermore, CM often remits to EM with a transition rate of 26%, considered a transition time of 2 years [62].

3.3. Alteration of white matter in migraine sufferers

Taking into account all the scientific investigations that have been performed in the past, migraine has been considered to be a neurovascular disorder that does not include long-term consequences to the brain [63]. Numerous studies suggested the existence of associations between clinical stroke, migraine, and white matter hyperintense lesions. Although due to the lack of specificity of the methods used so far, no definite conclusion related to the topic has been reached. In Mark C. Kruit et al., 2005 [63], it has been demonstrated that brain infarction occurs far more frequently than expected in migraine patients. More

importantly, the influence of migraine severity (attack frequency) on the risk of the presence of lesions is suggesting the existence of a causal relationship between migraine severity and lesion load. In another study, performed with MRI (Alyx Porter et., al, 2005 [64]), it has been confirmed that patients with migraine are at increased risk for White Matter Hyperintensities (WMH), although the pathophysiology and long-term consequences of these lesions are still unknown. Furthermore, it has been stated that white matter lesions in migraineurs could be linked to underlying diseases such as cerebral autosomal dominant arteriopathy with subcortical infarcts and leukoencephalopathy (CADASIL), central nervous system vasculitis, or mitochondrial encephalopathy with lactic acidosis and stroke-like episodes (MELAS). To be specific, within the topic related to WMH, in Ali G. Hamedani et., al, 2013 [65], this has been associated with migraine in terms of volume cross-sectionally but not in terms of its progression over time.

It is also important to report some conclusions that have been obtained by using DTI techniques. One of the most important studies that have been conducted on this topic, Catherine D. Chong et., al, 2015 [66], enlighten the areas of the brain in which some differences with respect to healthy control subjects in terms of MD, RD and FA have been detected. Indeed, migraine patients showed greater MD in the left and right anterior thalamic radiations, the left corticospinal tract, and the right inferior longitudinal fasciculus tract [66]. Regarding the RD, migraine patients showed greater RD values in the left anterior thalamic radiations, the left corticospinal tract as well as the left and right inferior longitudinal fasciculus tracts. For the FA, no differences have been identified for any tracts. According to the authors, these results are indicating that white-matter integrity could be altered in migraine and that migraine history could be positively correlated with greater alterations in tract integrity [66].

In Lars Neeb et al [67], instead, some significant differences related to the parameter FA have been found in the comparison between EM patients and controls. In particular, it has been shown that EM patients present lower FA values in the left Superior longitudinal fasciculus and higher FA values in the right Inferior fronto-occipital fasciculus compared to controls [67].

Considering the study conducted by Álvaro Planchuelo-Gómez et al [68], in the comparison between EM patients and controls with a TBSS analysis, it has been found that in EM patients some brain regions present increased AD values compared to controls. These statistical differences have been found in both right and left side of the following regions: External capsule, Posterior limb of internal capsule, Retrolenticular part of internal capsule, Sagittal stratum, Posterior thalamic radiation and Cerebral peduncle [68].

Additionally, in Rahil Rahimi et al [69], with the comparison between patients presenting migraine headache and controls (using the DTI model), it has been shown that WM

changes are mainly present in corpus callosum, cingulate fibers, brainstem, thalamic radiations, and superior and inferior longitudinal fasciculus.
Besides DTI, other diffusion models have been used to analyze the alteration of WM in EM patients.
For instance, ensemble average diffusion propagator measures obtained with Apparent measures using reduced acquisitions (AMURA) has been employed by Álvaro Planchuelo-Gómez et al [70] in EM with the purpose of overcome DTI measures. In the mentioned study, it has been found a decreased Return-to-origin Probability (RTOP) value for EM patients compared to healthy controls in 24 WM tracts, including anterior thalamic radiation, forceps minor, inferior fronto-occipital fasciculus and many more.
Also DKI model has been used to detect some differences between migraine patients and healthy controls. Particularly, in the study conducted by Kenji Ito et al [71], no significant differences in the DKI metrics of WM structures between EM patients and healthy controls. Although, they were able to detect increased values of Mean Kurtosis (MK) and MD in the periaqueductal gray matter (PAG) of EM patients compared to controls.
All these results led the author of this work to specifically analyze the brain areas in which these important differences have been found. Although, as mentioned before, the values reported by DTI are not the same as the ones that are reported by NODDI. For this reason, being critical in the evaluation of the obtained results is a crucial aspect on these occasions.

4 | NODDI Application in Episodic Migraine

In this chapter, the feasibility of translating the NODDI model into the in-vivo WM study for EM patients has been evaluated. In particular, a quantitative analysis has been performed in order to enlighten the differences between the white matter of subjects without the pathology (controls) and the ones affected by EM (patients).

4.1. Participants

A total of 23 subjects have been considered for the first TBSS analysis, 14 controls and 9 Episodic Migraine patients. It is important to specify the fact that all the subjects are women. Table 4.1 shows some additional information related to the considered subjects.

Table 4.1: Subjects' information: number of controls and EM patients, average age and number of subjects using contraceptives (pills or rings).

	Controls	**EM patients**
Number of Subjects	14 (60.87%)	9 (39.13%)
Average age (years)	30.92 ± 6.84	34.11 ± 7.73
Use of Contraceptive (pill/ring)	5/14 (35.71%)	5/9 (55.55%)

For the followed ROI analysis, it has been possible to add one EM patient to the dataset, due to the fact that the acquisition of the data was still ongoing. Thus, Table 4.2 shows the updated information for each group of subjects.

Table 4.2: Subjects' information: number of controls and EM patients, average age and number of subjects using contraceptives (pills or rings).

	Controls	**EM patients**
Number of Subjects	14 (58.33%)	10 (41.67%)
Average age (years)	30.92 ± 6.84	35.3 ± 8.15
Use of Contraceptive (pill/ring)	5/14 (35.71%)	6/10 (60%)

It is essential to specify the reason why women have been chosen for this research. In order to perform the acquisition at the exact time of the migraine attack, it is necessary to choose a condition that allows the scientists to do that. Here, the menstrual migraine case has been considered. The migraine attacks caused by this pathology occur regularly at menstruation and it is easier for the subjects to understand the time in which they could potentially experience the attack.
Regarding the control individuals, the brain activity was measured in two different conditions:

- Premenstrual;
- Midcycle.

The brain activity of the EM patients, instead, was measured in four phases (as shown in Figure 4.1):

- Interictal: in between two different seizures;
- Preictal: before the start of the seizure;
- Ictal: during the seizure;
- Postictal: after the seizure.

Electroencephalogram (EEG) acquisition is needed in order to distinguish the aforementioned phases of the EM patients' brain activity. It is possible to achieve this by using a specific algorithm, as mentioned in Ahmad Chamseddine et al [72]. The algorithm includes six essential stages, which are: data acquisition, preprocessing, feature extraction, features selection, classification and regularization [73]. To resume, at first, the EEG signal is collected by scalp or intracranial electrodes. Then, the raw data is filtered and segmented into several windows where each segment will be classified as interictal, preictal, ictal or postictal and independently processed. Afterwards, several linear/non-linear features are extracted. Then, linear or non-linear classifier are used in order to discriminate the reduce space dimension where the selected features are presented. Finally, trained

classifiers are used and a final regularization is performed in order to contextualize the predicted classes of successive windows.
It is necessary to bear in mind that, in some cases, it has been hard to collect all the measures for all the phases. Indeed, some EM patients won't present the data for all 4 phases.

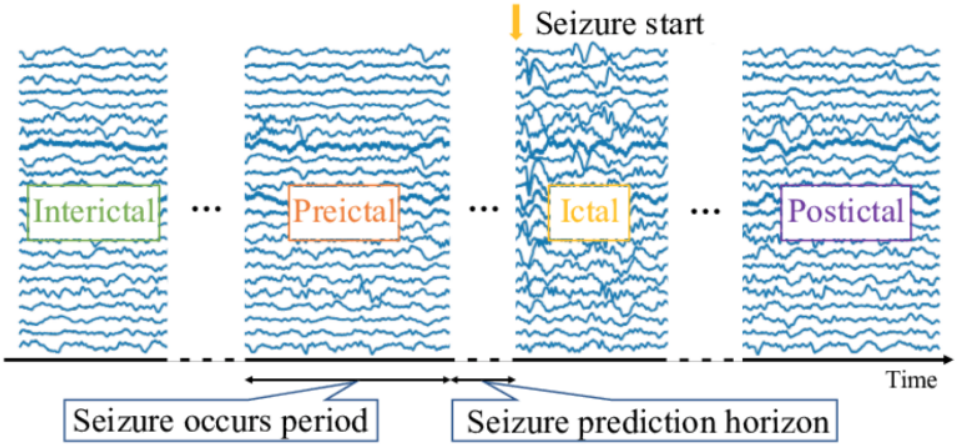

Figure 4.1: Illustration of the data acquisition of the Episodic Migraine Patients. [74]

It is important to understand that the control group has been only studied in two sessions, while the patient group has been studied in four sessions, which corresponds to the migraine cycle, as mentioned before. The premenstrual session should control the variations derived from the cycle itself compared to the preictal, ictal, and postictal sessions. The midcycle session should control the variations inherent to the cycle compared to the interictal session.

4.2. Image Acquisition

Both control and patient participants were scanned using a 3T Siemens Vida System scan with a 64-channel RF-receive head coil with the following parameters: TR=6800, TE=89ms, 66 slices, in-plane GRAPPA (parallel imaging) factor 2, Simultaneous multi-slice (SMS) factor 3, 2mm isotropic resolution. The sampling scheme included three diffusion shells with b=400, 1000, 2000s/mm2 along 32, 32, 60 gradient directions, respectively, and 8 non-diffusion-weighted volumes. The data preprocessing was done following the DESIGNER pipeline that has been found in Ades-Aron et. al. [75]. The data analysed throughout this thesis was acquired in the context of the Project MIG_N2Treat

(Multimodal neuroimaging biomarkers through the migraine cycle) by the LASEEB research team. Furthermoe, the preprocessing of the diffusion MRI data was performed by a member of the team. All the MRI and EEG data have been collected at Hospital da Luz of Lisbon.

4.3. AMICO framework

During this thesis, different approaches have been used. We started with the application of the NODDI MatLab toolbox [76], but it has been noticed that the MatLab toolbox requires an extremely long time to perform the acquisition. The processing time of this toolbox is related to the available performance cluster. The machine that has been used to apply the model has just 8 cores and, moreover, the number of voxels required to complete a whole-brain analysis is very high. Thus, it has been seen that the time required for the data processing of a single subject was approximately 3 days. This is due to the fact that NODDI can be considered a computationally very expensive non-linear procedure [77]. Hence, the author felt the need to find a solution in order to reduce the acquisition time and complete the NODDI fitting of all the considered data. To accelerate the NODDI fitting, a new framework called Accelerated Microstructure Imaging via Convex Optimization (AMICO) was applied. Indeed, AMICO is a framework that has been reformulated in order to assume a convenient linear structure that can be easily solved by the use of fast algorithms [77]. It has been demonstrated that AMICO represents an effective means to drastically accelerate the NODDI fit while preserving precision and accuracy in the estimated model parameters [77]. Due to the applied linearity, it is possible to accelerate the fitting process up to four orders of magnitude with respect to non-linear procedures like NODDI. Therefore, within the application of AMICO, it was noticed that the required time for a single folder changed from 3 days to 35 minutes. This clearly demonstrates the advantage of AMICO over the standard fitting, especially when the analysis of a rich dataset is required.
Finally, the AMICO framework has been applied to our dataset [78]. The framework was implemented in Python, contrary to the original NODDI model which was applied using Matlab.

4.4. TBSS

TBSS has been used to identify the whole brain white matter microstructural changes using AMICO in Episodic Migraineurs compared to the control subjects [79]. The white matter skeleton was created based on the mean FA map of the whole cohort. Then, in or-

der to enlighten which FA skeleton voxels are significantly different between two groups of subjects, the voxelwise statistics on the skeletonized FA data were applied, using a t-test. Successively, the NODDI metrics maps were projected onto the skeleton. In particular, TBSS has been applied for Orientation Dispersion (OD), ISOVF, and ICVF, which are the most relevant parameters for the case of study, obtained with the application of AMICO.

As mentioned in section 2.4, the OD is related to the degree of dispersion of the dendrites. The ICVF or NDI represents the packing of the density of axons and dendrites. In contrast, the ISOVF or FWF represents the extent of contamination caused by CSF and it can be defined as the ratio between the Free water (FW) volume in the voxel and the total voxel volume.

Once the application of TBSS in these parameters was made, the author proceeded with the comparison between controls and patients for all the aforementioned parameters, in order to determine the principal voxels that present a drastic statistical difference. This led us to determine the brain areas in which it is possible to find an alteration of the white matter.

4.5. Region-of-interest (ROI) Analysis

ROI analysis has been applied considering the results that have been obtained with the TBSS analysis in order to further test the suitability of NODDI in the case of EM.

4.5.1. ROI Analysis' advantages

In Russell A. Poldrack et al. and Martijn Froeling et al. [80, 81] it is possible to comprehend the primary benefits of using the ROI analysis instead of other Image Analysis techniques for Diffusion MRI.
One of the reasons is related to the control of the Type 1 error (false-positive). This is the error that occurs if an investigator is rejecting a null hypothesis that is true in the population [82]. Hence, Type 1 error is related to the false-positive results. With the ROI analysis, it is possible to limit the number of statistical tests to a few ROIs instead of testing in a large number of voxels in the cases in which a clear hypothesis about the expected differences in white matter in a well-defined region of the brain has been already stated [81]. Indeed, based on the results that had been obtained in the previous work (with a voxelwise approach), the author already knew what are the WM tracts that presented significant differences between controls and MM patients. For this reason, it was

possible to limit our research to the ROIs that are involved in the area selected before, and hence it was possible to reduce the total number of statistical tests, reducing the aforementioned Type 1 error.
Furthermore, ROI analysis could be preferred to other Image analysis techniques, especially when the available datasets present complex designs, where there are multiple conditions or variables to compare. Indeed, within the use of an ROI analysis it is easy to plot and compare the signals that are coming from the areas of interest for different conditions and variables [80]. In our specific case, this type of analysis could be really useful, since we present a small dataset with multiple conditions to analyze and compare, as it will be shown in subchapter **??**.
Considering all this information, the ROI analysis could be considered a method that is highly sensitive to small changes in the parameters of interest and relatively easy to use. Furthermore, this technique doesn't require high technical knowledge compared to other techniques [81].

4.5.2. ROI Analysis' disadvantages

It is essential to understand that ROI analysis cannot be used in every circumstance. Indeed, it has been stated that this method cannot be used if there is no hypothesis about the location of the effects in the brain caused by the pathology of interest [81]. Indeed, this type of technique is very time-consuming and hence it is not suitable for a whole-brain analysis. Furthermore, performing an ROI analysis requires at least a moderate knowledge of brain anatomy, and even with a presumptive ROI definition and advanced knowledge of the anatomy, this technique may exhibit high intra- and inter-user variability. Moreover, another disadvantage of ROI analysis could be related to the loss of spatial resolution in the detection map.

4.5.3. Definition of ROIs

ROIs could be defined in several ways: manual delineation, using tractography, using WM atlases, and plenty more.
The first method is the manual delineation, which consists of the manual drawing of the ROI on a structural MRI image. In this method, the investigator has to have a clear idea of what the borders of the regions correspond to and to what extent they should be included [81]. For this reason, the accuracy of the method fully depends on the experience and anatomical knowledge of the investigator that is performing the drawing. Furthermore, it has to be taken into account that the ROI size should be different for each subject. Indeed, this method could be extremely subjective and time-consuming.

In order to overcome this problem, the ROIs can be defined based on WM atlases. These are multiple predefined atlases of WM, created by experts with a well-defined neuroanatomy background. Thus, these atlases could theoretically minimize the lack of knowledge of the ones that are performing the study, and they can improve the comparability of findings across studies. In the case of the WM, the most well-known atlases are the Johns Hopkins University (JHU) atlas and the probabilistic Juelich atlas.
It is also important to specify that investigators must be aware of possible overlaps between different regions with the data under study due to the fact that misalignment could obscure region locations [81].

JHU-ICBM white-matter labels atlas and tractography atlases

In this work, the author decided to perform the ROI analysis using WM atlases. In particular, the JHU-ICBM white-matter labels and tractography atlases have been used to identify the WM structures that have been previously selected in the past study.
Figure 4.2 shows the JHU-ICBM-labels-1mm and JHU-ICBM-labels-2mmWM atlases, in which it is possible to find 48 WM tract labels that were created by hand segmentation of a standard-space average of dMRI tensor maps taken from an investigation of 81 subjects [83]. The JHU-ICBM-labels-1mm has been chosen in this work.

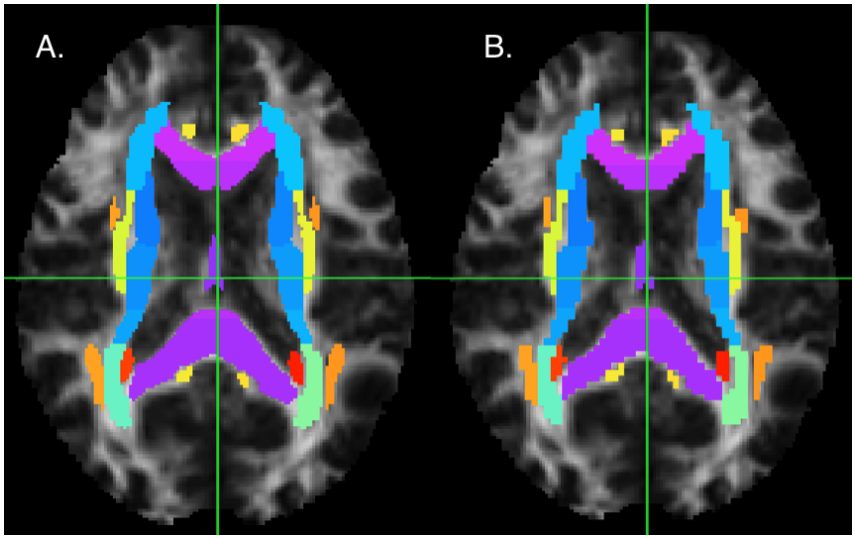

Figure 4.2: Illustration of the Johns Hopkins University (JHU) white-matter labels atlas. A. JHU-ICBM-labels-1mm atlas. B. JHU-ICBM-labels-1mm atlas. Location: z=45 in both images. Each color is associated with a label. In total there are 48 labels associated to 48 different WM structures.

Figure 4.3 shows the WM tractography atlases, which are JHU-ICBM-tracts-maxprob-thr0-1mm, JHU-ICBM-tracts-maxprob-thr25-1mm and JHU-ICBM-tracts-maxprob-thr50-1mm. These atlases identify in a probabilistic way 20 structures that have been obtained by averaging the results of running deterministic tractography on 28 subjects [83]. JHU-ICBM-tracts-maxprob-thr0-1mm atlas has been used in this work to identify the WM tracts that were not available in the JHU-ICBM-labels-1mm atlas. Moreover, JHU-ICBM-tracts-maxprob-thr0-1mm compared to the other 2 in figure 4.3 is the one with the smallest threshold related to the location probability of the single ROIs (0% of threshold). This means that, using this atlas, it is possible to achieve results also in points that are located between two different regions, because it is less limited than the other two. Even if JHU-ICBM-tracts-maxprob-thr25-1mm (25% of threshold) and JHU-ICBM-tracts-maxprob-thr50-1mm (50% of threshold) are more accurate in terms of ROIs location, with the use of these 2 atlases, it is not possible to visualize points that are in between different regions. From the results that have been obtained with the voxelwise method in the past study, the author noticed that the WM areas where significant differences were found included a lot of points that were located in between different WM tracts. For this reason, the JHU-ICBM-tracts-maxprob-thr0-1mm atlas was considered as the most suitable atlas for the purpose of the study.

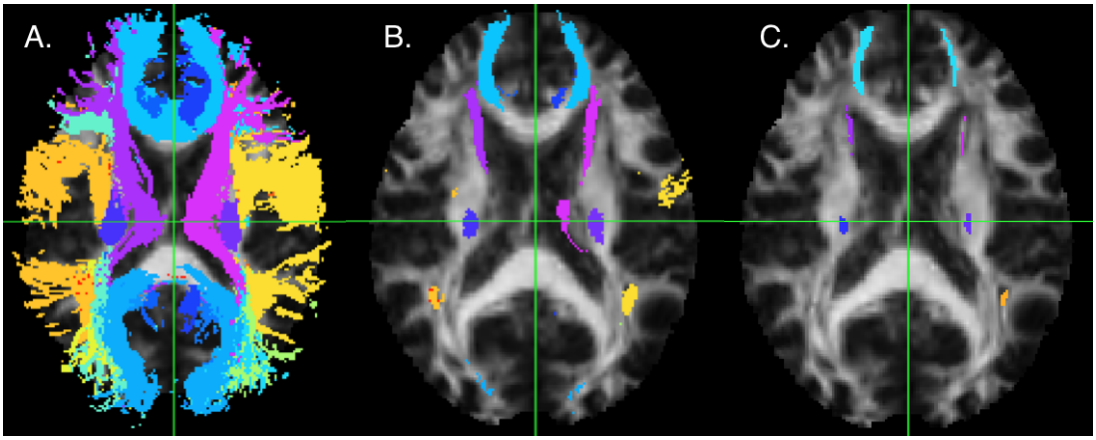

Figure 4.3: Illustration of the Johns Hopkins University (JHU) WM tractography atlases, identifying in a probabilistic way 20 WM tracts. A. JHU-ICBM-tracts-maxprob-thr0-1mm atlas, ROI location threshold of 0%. B. JHU-ICBM-tracts-maxprob-thr25-1mm atlas, ROI location threshold of 25%. C. JHU-ICBM-tracts-maxprob-thr50-1mm atlas, ROI location threshold of 50%. Location: z=45 for all the 3 atlases. Each color is associated with a particular WM tract.

5 | Results

5.1. Results from TBSS analysis

As mentioned before, not all the subjects in the patient group present the acquisition for all phases, due to the fact that the acquisitions are still ongoing and due to the restricted available time that the author had during the research work. Indeed, for the phases connected to the migraine cycle itself, only the postictal phase and interictal phase have been chosen to perform the comparisons with the control subjects. This is due to the fact that the postictal and interictal phases acquisitions were the most abundant throughout all subjects in the patient group. Thus, this choice allows the author to have an higher number of subjects for the analysis (higher than the case of choosing just the ictal or preictal phase sessions). Ideally, it is better to consider all three phases connected to the premenstrual phase in order to have a solid statistical analysis.
As mentioned before, the postictal session (which is part of the migraine cycle) is controlled for the premenstrual phase of control subjects, while the interictal session is controlled for the midcycle phase of control subjects. Thus, in order to highlight the differences between controls and EM patients for the parameters OD, ICVF and ISOVF, two comparisons have been performed (using a TBSS analysis):

- premenstrual-postictal;
- midcycle-interictal.

Furthermore, in order to highlight the intra-phase differences in controls and EM patients for the aforementioned parameters, two other comparisons have been performed (using as well TBSS analysis):

- interictal-postictal;
- midcycle-premenstrual.

The age of all the subjects was inserted in the design matrix, and, hence, considered in the analysis.
As a point of example, Figure 5.1 reports the ISOVF, ICVF and OD parametric maps

of the aforementioned comparison between one control subject in midcycle session and one EM patient in interictal session. This could give an idea of how the 3 parameters vary in the different WM tracts for both categories of subjects. Considering the same control subject and the same EM patient, also the the parametric maps for the comparisons premenstrual-postictal, mydcycle-premenstrual and interictal-postictal have been reported in Figure 5.2, Figure 5.3 and Figure 5.4, respectively.
The comparison midcycle-premenstrual highlights the possible differences that could occur in the same control subject during different phases (Figure 5.3). It is possible to state the same for the comparison interictal-posictal, for the case of an EM patient. As it is possible to notice, the parametric maps are slightly changed when two different phases are considered. Thus, the intra-phase differences for both control and patient are not so evident.
It is possible to notice some differences between control and patient in Figure 5.1 and Figure 5.2. However, this is the comparison between just one control subject and one patient and, for this reason, it is not possible to assume it as a valid result. Therefore, the TBSS analysis has been applied, in order to involve all the subjects that are present in our database and, hence, improve the accuracy of the results.

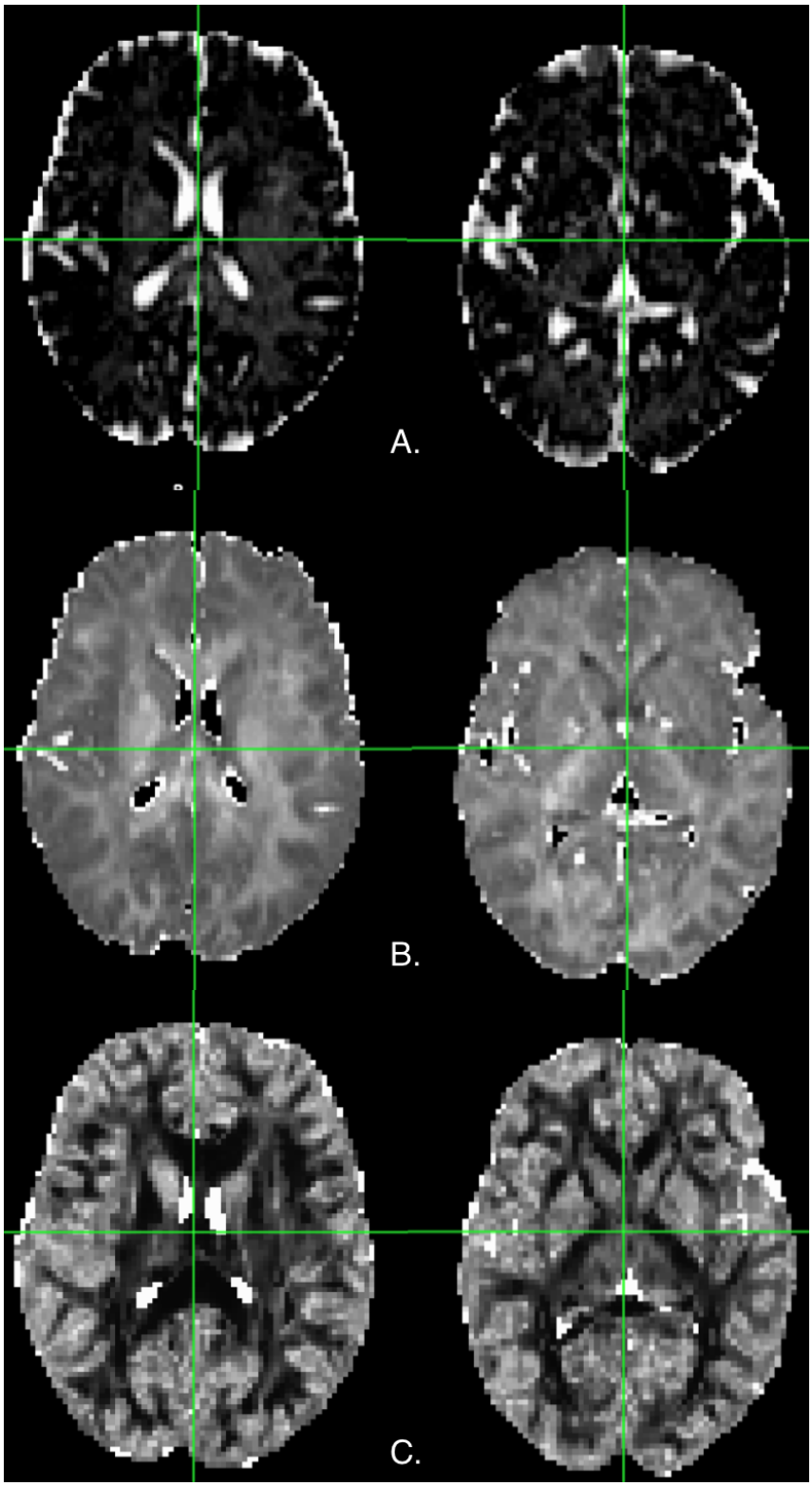

Figure 5.1: ISOVF (A.), ICVF (B.) and OD (C.) parametric maps for one control subject during the midcycle phase (left) and for one EM patient during the interictal phase (right). ISOVF, ICVF and OD intensities are varying from 0 to 1.

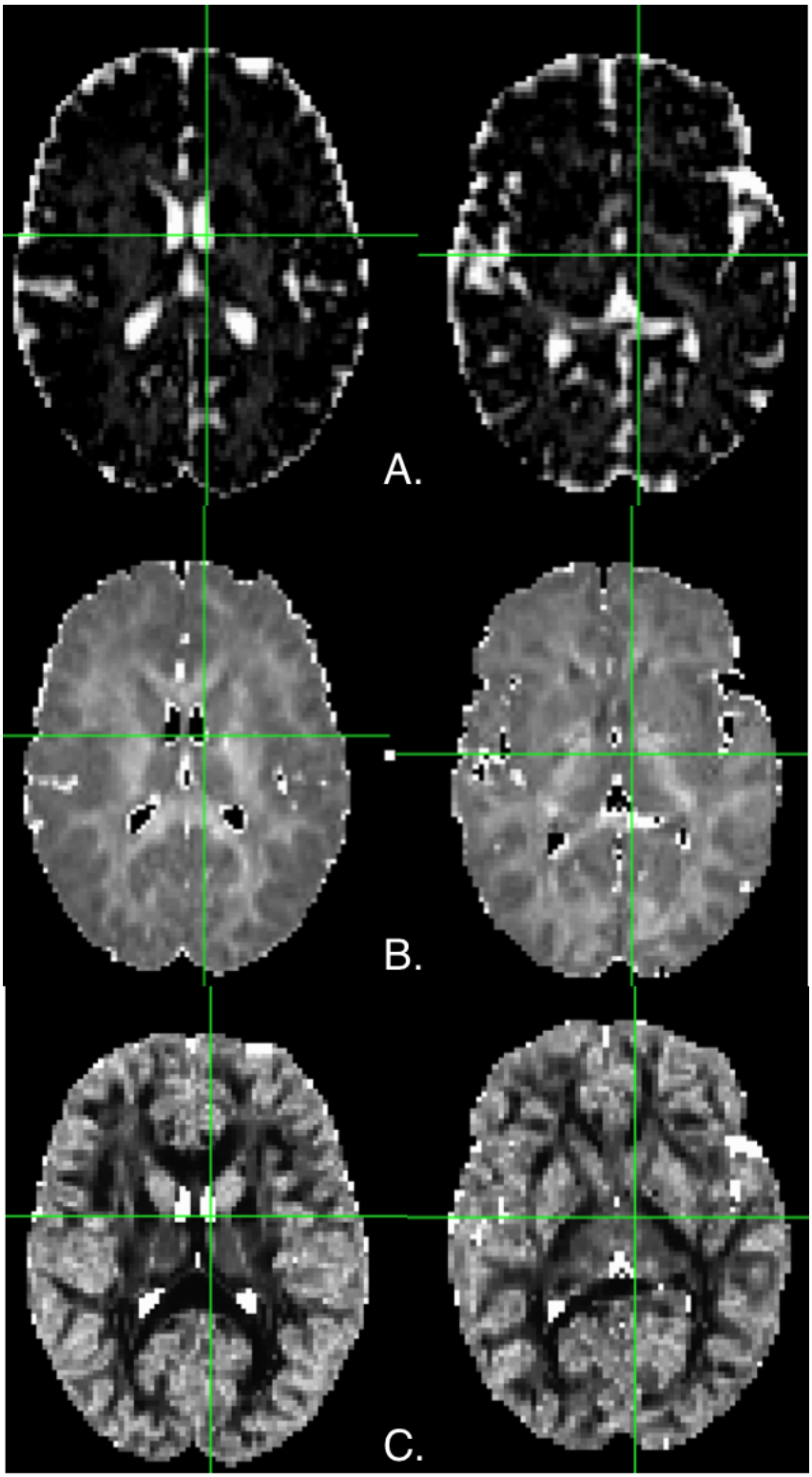

Figure 5.2: ISOVF (A.), ICVF (B.) and OD (C.) parametric maps for one control subject during the premenstrual phase (left) and for one EM patient during the postictal phase (right). ISOVF, ICVF and OD intensities are varying from 0 to 1.

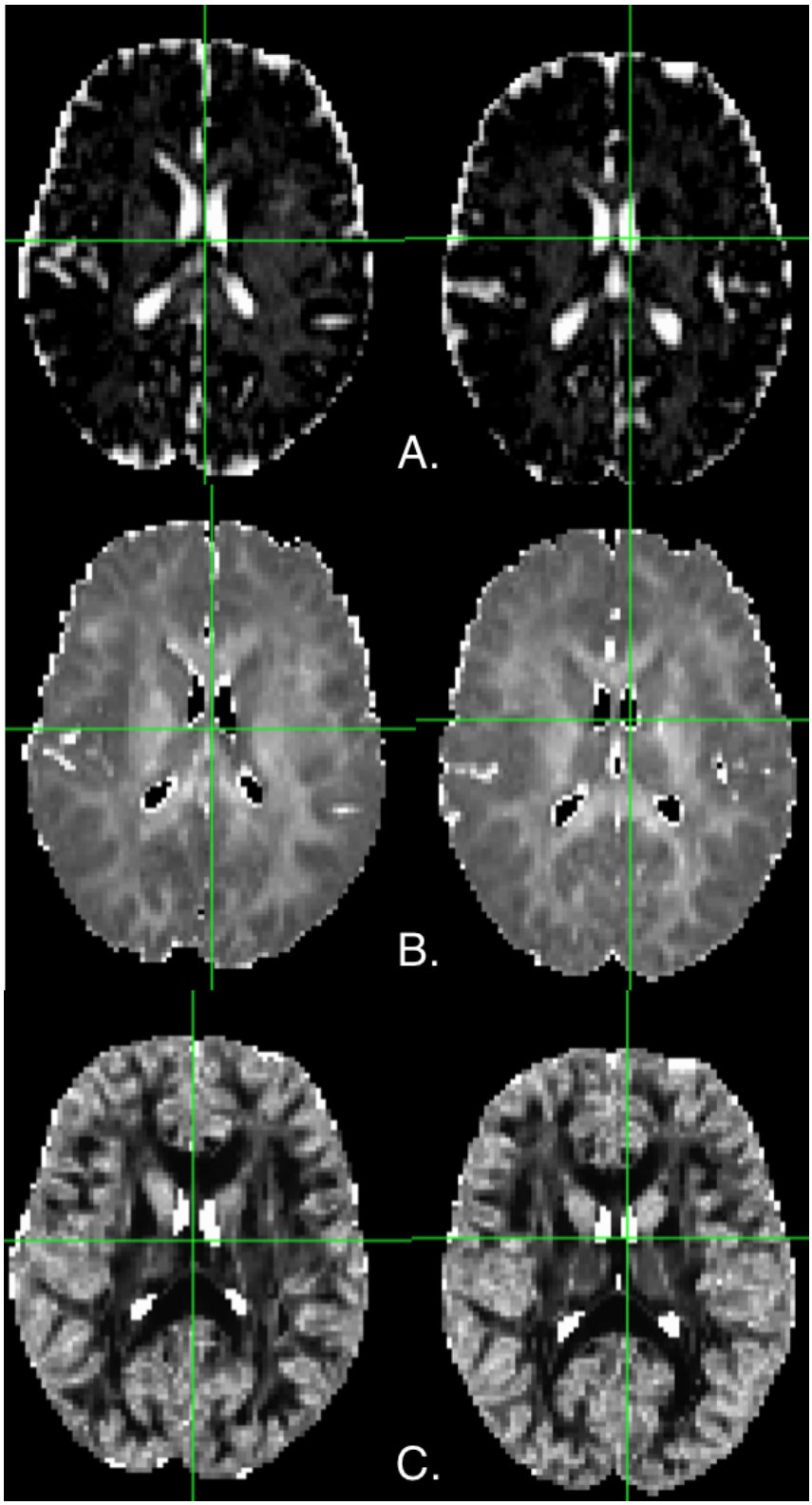

Figure 5.3: ISOVF (A.), ICVF (B.) and OD (C.) parametric maps for one control subject during the midcycle (left) and premenstrual (right) phases. ISOVF, ICVF and OD intensities are varying from 0 to 1.

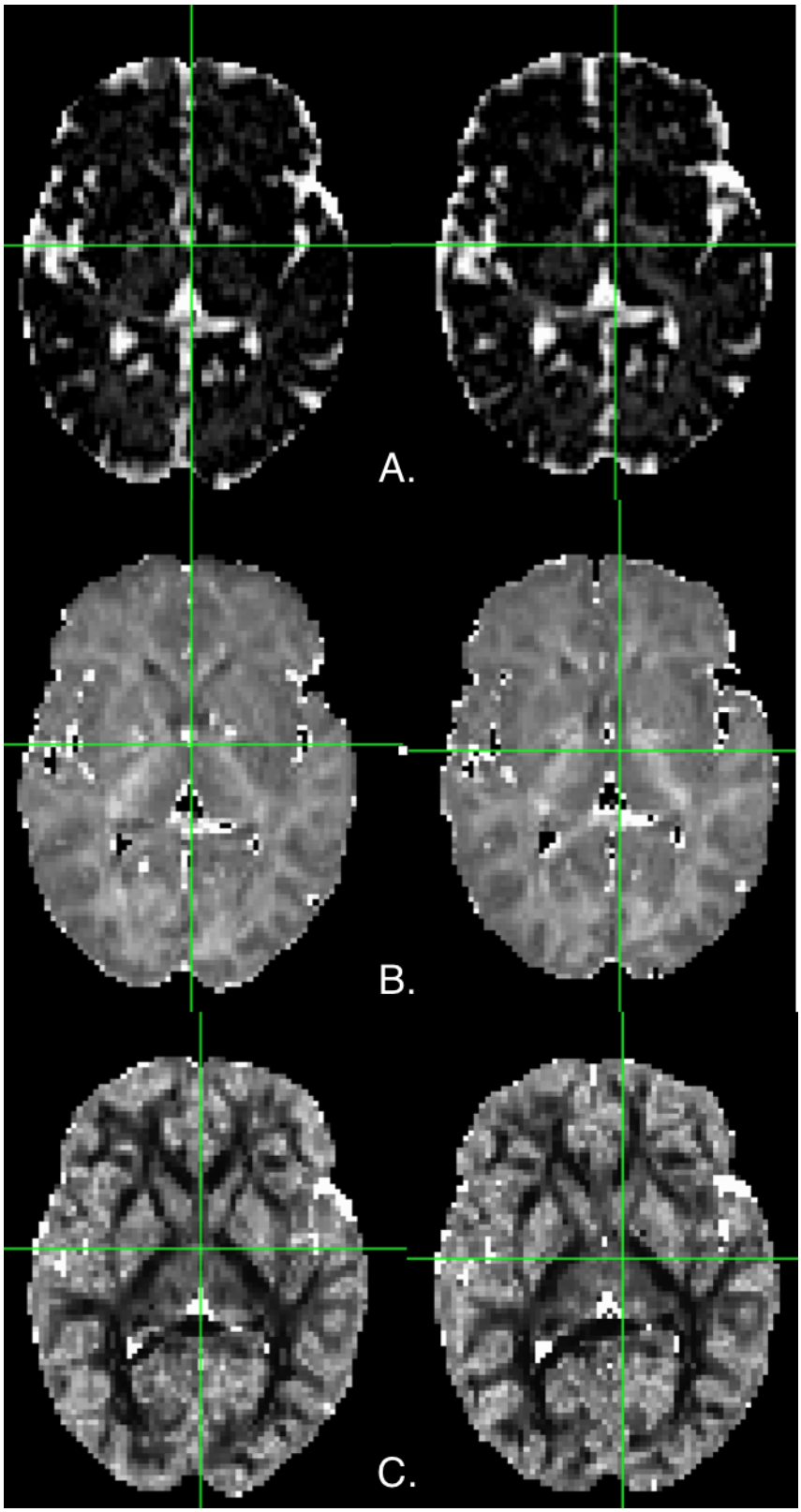

Figure 5.4: ISOVF (A.), ICVF (B.) and OD (C.) parametric maps for one EM patient during the interictal (left) and posictal (right) phases. ISOVF, ICVF and OD intensities are varying from 0 to 1.

In the performed TBSS analysis, no significant differences were found in the premenstrual-postictal, interictal-postictal, and midcycle-premenstrual comparisons.
Regarding the midcycle-interictal comparison, some significant results have been found only for the ISOVF parameter, as shown in Table 5.1. The whole-brain white matter analysis of NODDI metrics revealed a reduced value of ISOVF in the interictal phase compared to the midcycle phase in the left inferior fronto-occipital fasciculus, left forceps major, left superior longitudinal fasciculus, and left cingulum.

Table 5.1: White Matter regions where significantly decreased ISOVF values were found in EM patients during the interictal phase compared to controls during midcycle phase. The maximum significant Threshold-Free Cluster Enhancement (TFCE) uncorrected p-value is 0.048. Only the regions with a p-value lower than 0.05 are included in this table. L Left, R Right, EM Episodic Migraineurs, CTRL controls.

Comparisons	**White Matter tract**	**Averaged p-value (uncorrected)**
EM<CTRL	Inferior Fronto-Occipital Fasciculus L	0.048
EM<CTRL	Forceps Major L	0.036
EM<CTRL	Superior Longitudinal Fasciculus L	0.044
EM<CTRL	Cingulum L	0.038

In Figure 5.5, it is possible to visualize the areas in which significantly decreased ISOVF values in the interictal phase compared to the midcycle phase have been found for different values of z (Axial Plane representation). Figure 5.6 and Figure 5.7 show that no significant differences between controls in midcycle phase and EM patients in interictal phase have been identified for the parameters ICVF and OD.

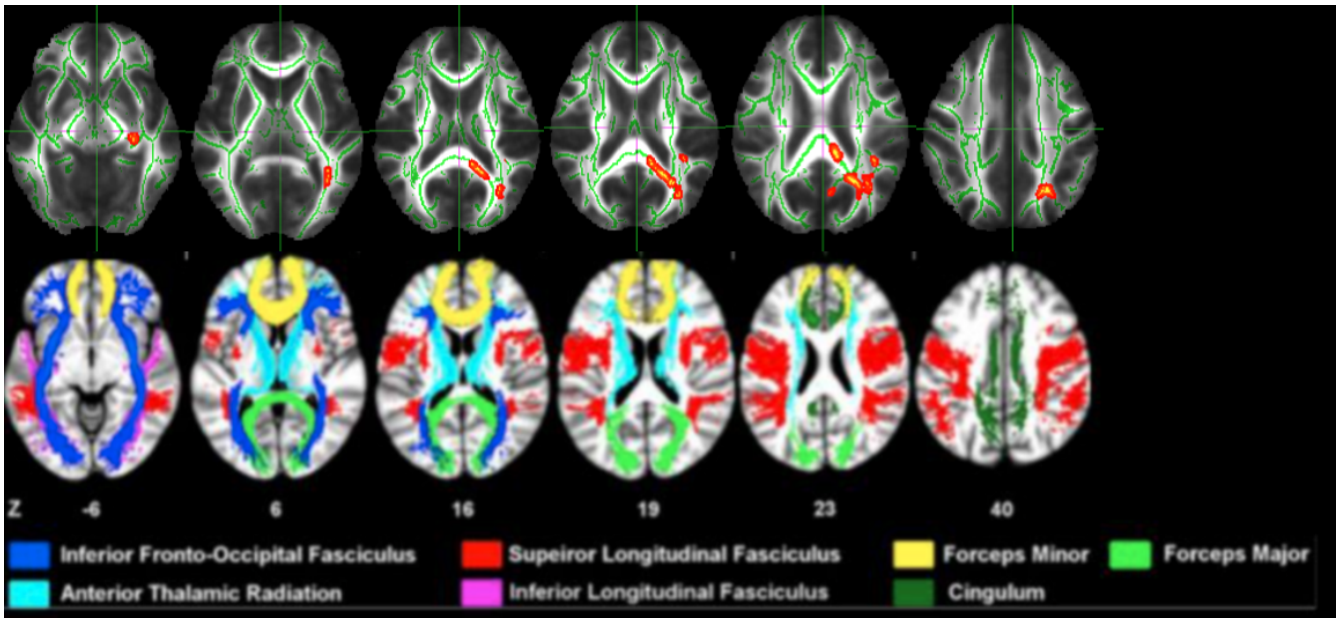

Figure 5.5: Up: White Matter regions where significantly decreased ISOVF values were found in the interictal phase compared to the midcycle phase for different z values (-6, 6, 16, 19, 23, 40). The white-matter skeleton is represented in green. Significantly decreased ISOVF values are represented with red-yellow clusters. L left hemisphere, R right hemisphere. Down: White-matter tracts using the Johns Hopkins University (JHU) white-matter tractography atlas. Color labels for the JHU tracts are displayed at the bottom. [84]

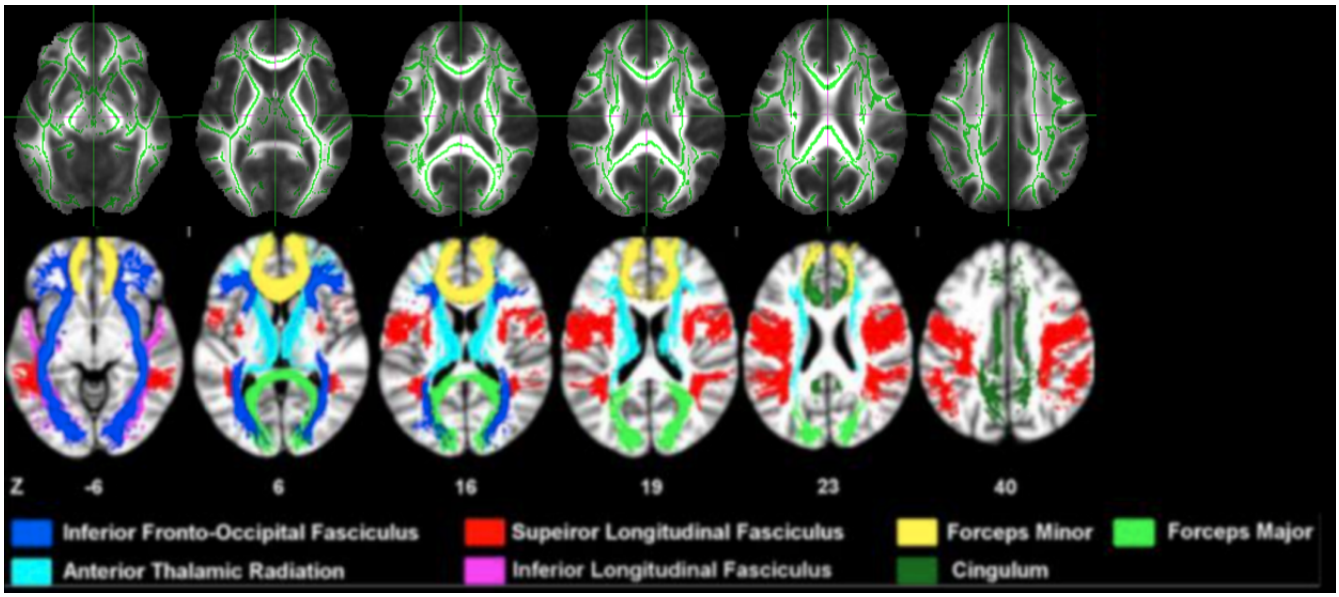

Figure 5.6: Up: White Matter regions where significantly decreased ICVF values were found in the interictal phase compared to the midcycle phase for different z values (-6, 6, 16, 19, 23, 40). The white-matter skeleton is represented in green. Significantly decreased ICVF values are represented with red-yellow clusters. No significant differences have been identified in this comparison for the parameter ICVF. L left hemisphere, R right hemisphere. Down: White-matter tracts using the Johns Hopkins University (JHU) white-matter tractography atlas. Color labels for the JHU tracts are displayed at the bottom. [84]

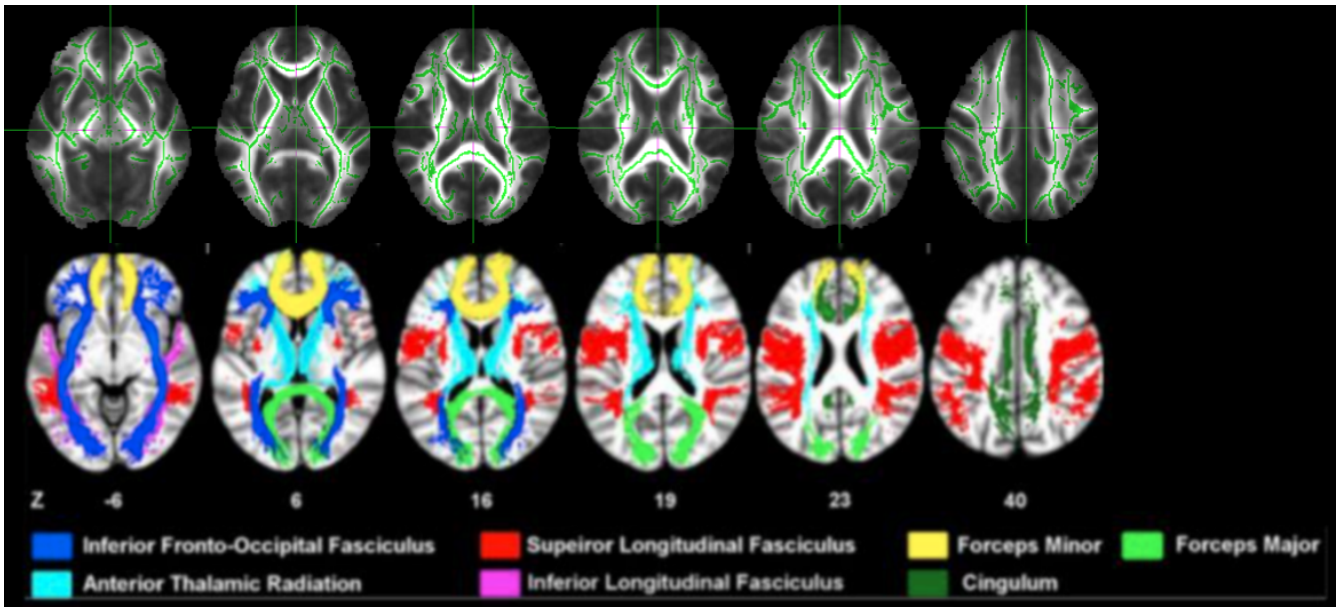

Figure 5.7: Up: White Matter regions where significantly decreased OD values were found in the interictal phase compared to the midcycle phase for different z values (-6, 6, 16, 19, 23, 40). The white-matter skeleton is represented in green. Significantly decreased OD values are represented with red-yellow clusters. No significant differences have been identified in this comparison for the parameter OD. L left hemisphere, R right hemisphere. Down: White-matter tracts using the Johns Hopkins University (JHU) white-matter tractography atlas. Color labels for the JHU tracts are displayed at the bottom. [84]

5.2. Results from ROI analysis

Based on the TBSS results, the author tried to identify the ROIs that are included in the areas where this significant difference has been found by using the JHU atlases (mentioned in the subsection 4.5.3), with the purpose of deeply testing those areas and discovering other possible areas that could register significant differences among the different groups and parameters present in the available database, using the high sensitivity offered by the ROI analysis.

In particular, 10 WM structures and tracts have been identified with the use of the atlases JHU-ICBM-labels-1mm and JHU-ICBM-tracts-maxprob-thr0-1mm, as shown in Figure 5.8.

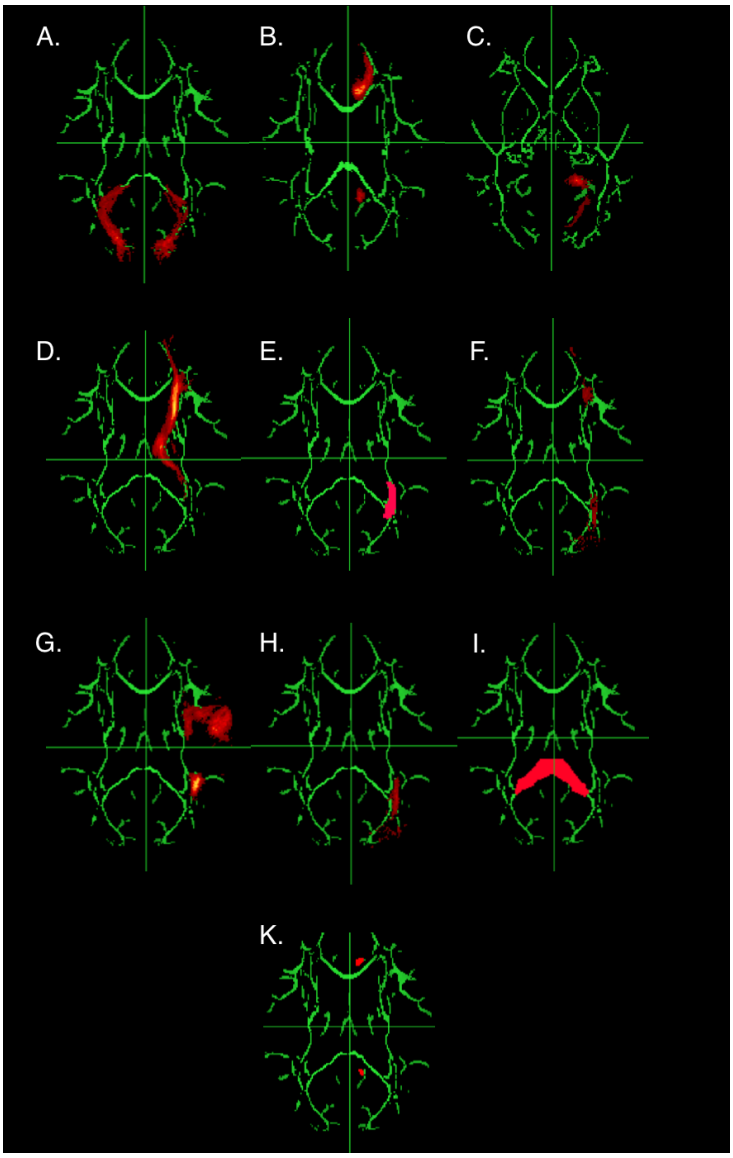

Figure 5.8: Illustration of the WM structures included in the investigation. A. Forceps major, JHU white-matter tractography atlas. Location: z=90. B Cingulum (cingulate gyrus) Left, JHU white-matter tractography atlas. Location: z=90. C. Cingulum (hippocampus) Left, JHU-ICBM-DTI-81 white-matter labels atlas. Location: z=70. D. Inferior fronto-occipital fasciculus Left, JHU white-matter tractography atlas. Location: z=90. E. Anterior thalamic radiation Left, JHU-ICBM-DTI-81 white-matter label atlas. Location: z=90. F. Posterior thalamic radiation Left, JHU white-matter tractography atlas. Location: z=90. G. Superior longitudinal fasciculus Left, JHU white-matter tractography atlas. Location: z=90. H. Inferior longitudinal fasciculus Left, JHU white-matter tractography atlas. Location: z=90. I. Splenium of corpus callosium Left, JHU-ICBM-DTI-81 white-matter labels atlas. Location: z=90. K. Posterior corona radiata Left, JHU-ICBM-DTI-81 white-matter label atlas. Location: z=100.

Once the ROIs have been identified, the author proceeded with the extraction of the single ROIs, centered on the skeletonized maps of the mean FA values for each group of subjects. Then, a t-test was applied for all the four aforementioned comparisons for the parameters ISOVF, ICVF and OD (significant difference if p-value$<$0.05).
Finally, Table 5.2, 5.3, 5.4 and 5.5 show the results that have been obtained at the end of the ROI analysis. It is important to specify that the multiple comparison correction for the p-values was not performed due to the fact that the obtained uncorrected p-values were too high to survive the correction and hence be classified as significant. Indeed, considering the Bonferroni correction method, in order to correct the p-value, it is necessary to multiply it by the total number of comparisons that have been performed. In this study, we performed 4 comparisons per each parameter (ISOVF, ICVF and OD) for a single WM structure. This means that if we are considering 10 WM structures, the total number of comparisons is $4 \times 3 \times 10 = 120$. Taking the smallest p-value obtained in the results (which is 0.0129) and multipling it by 120 (following the Bonferroni correction method), it is possible to see that even this value won't survive the correction because it won't be inferior to 0.05.

Table 5.2: Pair-wise comparisons of the uncorrected p-values of region-of-interest white matter tracts among different groups and parameters of interest (ISOVF, ICVF, OD).
L: left hemisphere. R: right hemisphere.
MID: Control subjects during midcycle phase. INT: MM patients during interictal phase.
*Significant differences (p$<$0.05) are marked with an asterisk.

WM tracts	Uncorrected p-values		
	MID-INT		
	ISOVF	ICVF	OD
Splenium of corpus callosium L	**0.02***	0.18	0.30
Anterior thalamic radiation (ATR) L	**0.02***	0.25	0.65
Posterior thalamic radiation (PTR) L	0.08	0.17	0.34
Posterior corona radiata (PCR) L	**0.03***	0.50	0.80
Inferior fronto-occipital fasciculus (IFOF) L	**0.04***	0.29	0.52
Cingulum (hippocampus) L	0.29	0.97	0.85
Cingulum (cingulate gyrus) L	0.11	0.43	0.60
Inferior longitudinal fasciculus (ILF) L	0.56	0.15	0.18
Superior longitudinal fasciculus (SLF) L	0.12	0.42	0.85
Forceps major	0.11	0.06	0.19

Table 5.3: Pair-wise comparisons of the uncorrected p-values of region-of-interest white matter tracts among different groups and parameters of interest (ISOVF, ICVF, OD).
L: left hemisphere. R: right hemisphere.
MID: Control subjects during midcycle phase. PRE: Control subjects during premenstrual phase.
*Significant differences ($p<0.05$) are marked with an asterisk.

WM tracts	Uncorrected p-values		
	MID-PRE		
	ISOVF	ICVF	OD
Splenium of corpus callosium L	0.44	0.53	0.27
Anterior thalamic radiation (ATR) L	0.90	0.57	0.20
Posterior thalamic radiation (PTR) L	0.38	0.37	0.24
Posterior corona radiata (PCR) L	**0.01***	0.79	0.23
Inferior fronto-occipital fasciculus (IFOF) L	0.73	0.62	0.21
Cingulum (hippocampus) L	0.70	0.87	0.28
Cingulum (cingulate gyrus) L	0.55	0.46	0.34
Inferior longitudinal fasciculus (ILF) L	0.12	0.55	0.21
Superior longitudinal fasciculus (SLF) L	**0.03***	0.80	0.28
Forceps major	0.98	0.62	0.27

Table 5.4: Pair-wise comparisons of the uncorrected p-values of region-of-interest white matter tracts among different groups and parameters of interest (ISOVF, ICVF, OD).
L: left hemisphere. R: right hemisphere.
POS: MM patients during postictal phase. PRE: Control subjects during premenstrual phase.
*Significant differences ($p<0.05$) are marked with an asterisk.

WM tracts	Uncorrected p-values		
	PRE-POS		
	ISOVF	ICVF	OD
Splenium of corpus callosium L	0.89	0.89	0.51
Anterior thalamic radiation (ATR) L	0.97	0.47	0.83
Posterior thalamic radiation (PTR) L	0.54	0.50	0.95
Posterior corona radiata (PCR) L	0.18	0.31	0.99
Inferior fronto-occipital fasciculus (IFOF) L	0.81	0.61	0.78
Cingulum (hippocampus) L	0.74	0.80	0.77
Cingulum (cingulate gyrus) L	0.40	0.23	0.44
Inferior longitudinal fasciculus (ILF) L	0.43	0.74	0.76
Superior longitudinal fasciculus (SLF) L	**0.03***	0.38	0.78
Forceps major	0.64	0.64	0.55

Table 5.5: Pair-wise comparisons of the uncorrected p-values of region-of-interest white matter tracts among different groups and parameters of interest (ISOVF, ICVF, OD).
L: left hemisphere. R: right hemisphere.
POS: MM patients during postictal phase. PRE: Control subjects during premenstrual phase.
*Significant differences ($p<0.05$) are marked with an asterisk.

WM tracts	Uncorrected p-values		
	INT-POS		
	ISOVF	ICVF	OD
Splenium of corpus callosium L	0.35	0.82	0.33
Anterior thalamic radiation (ATR) L	0.11	0.71	0.35
Posterior thalamic radiation (PTR) L	0.18	0.64	0.36
Posterior corona radiata (PCR) L	0.20	0.38	0.38
Inferior fronto-occipital fasciculus (IFOF) L	0.15	0.90	0.31
Cingulum (hippocampus) L	0.36	0.59	0.13
Cingulum (cingulate gyrus) L	0.64	0.99	0.31
Inferior longitudinal fasciculus (ILF) L	0.86	0.64	0.32
Superior longitudinal fasciculus (SLF) L	0.18	0.97	0.36
Forceps major	0.32	0.63	0.35

From the ROI analysis results, it is possible to state that significant results were registered in the left splenium of corpus callosum, left Anterior thalamic radiation (ATR), left Posterior corona radiata (PCR), left Inferior Fronto-Occipital Fasciculus (IFOF) and left SLF. In particular, in the left splenium of corpus callosum, a significant decrease of the ISOVF values of the MM patients under the interictal phase compared to the controls under the midcycle phase has been registered. The same result has been found in the left ATR and left IFOF. In the left PCR, significant differences of ISOVF values have been found for both midcycle-interictal and midcycle-premenstrual comparisons. Eventually, significant differences for the parameter ISOVF were found in both midcycle-premenstrual and premenstrual-posictal comparisons in the left SLF.

In Figure 5.9, we present the boxplots obtained in the comparison among different groups of subjects for the aforementioned WM tracts in which a significant difference had been registered. As it is possible to see, the comparisons marked with an asterisk are the ones that could be considered significant. Indeed, these comparisons do not reveal a huge overlap between the two boxplots. In the non-significant comparisons, it is possible to see

that the boxplots are mostly overlapped.

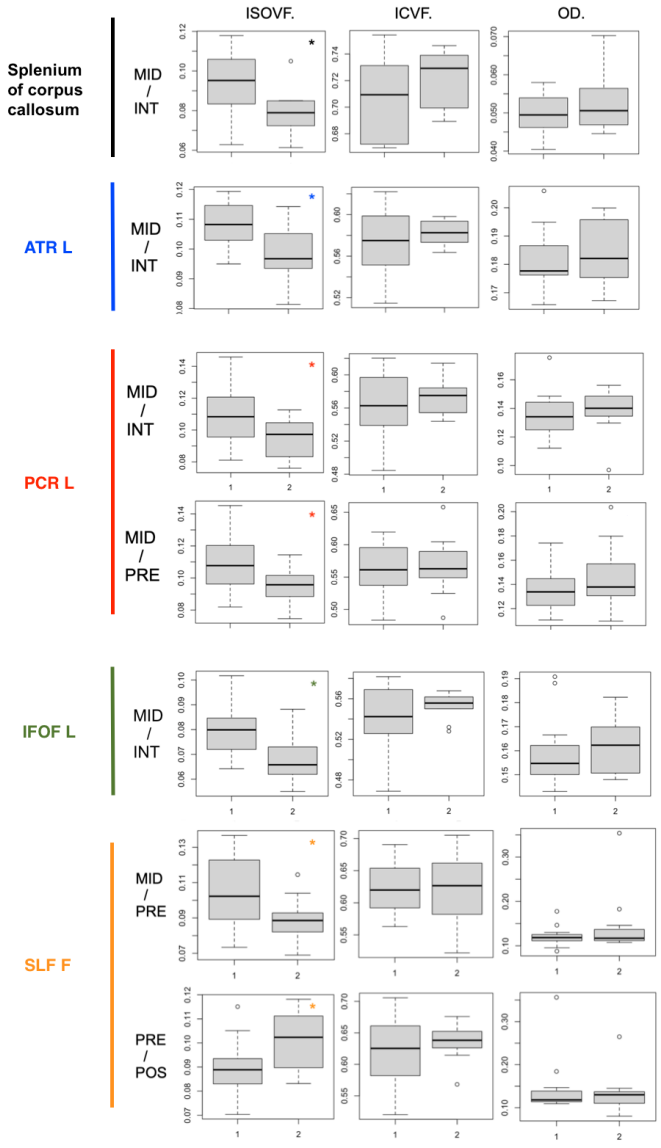

Figure 5.9: Illustration of the boxplots obtained in the comparison among different groups of subjects for the WM tracts in which a significant difference had been registered.
MID: Control subjects during midcycle phase. INT: MM patients during interictal phase. PRE: Control subjects during premenstrual phase. POS: MM patients during postictal phase.
L: left hemisphere. R: right hemisphere.
Group 1: midcycle. Group 2: interictal.
Splenium of corpus callosium. Group 1: midcycle. Group 2: interictal.
ATR: Anterior thalamic radiation. Group 1: midcycle. Group 2: interictal.
PCR: Posterior corona radiata. Up) Group 1: midcycle. Group 2: interictal. Down) Group 1: midcycle. Group 2: premenstrual.
IFOF: Inferior fronto-occipital fasciculus. Group 1: midcycle. Group 2: interictal.
SLF: Superior longitudinal fasciculus. Up) Group 1: midcycle. Group 2: premenstrual. Down) Group 1: premenstrual. Group 2: posictal.
*Boxplots with significant differences ($p<0.05$) are marked with an asterisk.

6 | Discussion

6.1. Discussion of the TBSS analysis results

In the present study, in order to have a larger number of patient subjects, just the postictal and the interictal phases were taken into account. Surely, the absence of significant results for most of the comparisons could be caused by several reasons. First of all, we could expect that the number of available subjects for this type of study is not high enough to determine relevant theories related to menstrual migraine. Indeed, this could also be a factor that can influence the results of the TBSS analysis. Second of all, it is also possible to assume that the NODDI model could simply not be adequate for this type of disorder. Further studies with larger samples are strongly suggested in order to determine something more related to the use of the NODDI model in migraine. It is crucial to bear in mind that with larger samples, the AMICO framework should be used in order to strongly optimize the time of the NODDI fitting, which could be extremely long especially in the case in which a larger number of subjects is considered.

Only for the comparison between the midcycle (control) and the interictal (patient) phases, some relevant white-matter alterations have been detected. Particularly, these are related to the parameter ISOVF (isotropic volume fraction) which indicates how much volume fraction of free water is present compared to the entire volume of a voxel. Indeed, it has been shown that in the interictal phase (migraineurs), there is a significant decrease in the ISOVF values compared to the midcycle phase (controls) in the left inferior fronto-occipital fasciculus, left forceps major, left superior longitudinal fasciculus, and left cingulum. This means that in those areas, the CSF volume is reduced compared to the control subjects. Intuitively, if the CSF volume is decreasing in a single voxel, it is expected that the ICVF (intracellular volume fraction) will increase. It is essential to bear in mind that ICVF or neurite density index (NDI) represents the packing of the density of axons and dendrites. Although, no significant differences between midcycle and interictal phases for the ICVF in those areas were registered. In order to understand the reason for this decrease in CSF volume in the aforementioned areas, it is crucial to clarify

the function that they are exercising.

Starting from the cingulum, this is considered one of the most distinctive fiber tracts in the brain, forming a near-complete ring from the orbital frontal cortices, along the dorsal surface of the corpus callosum, then down the temporal lobe towards the pole [85]. The white matter tract associated with the cingulum is called cingulum bundle (CB), which is related to emotion, executive control, episodic memory, and pain [85]. In particular, an alteration of this tract could be associated with functional memorization processes [86]. Indeed, it is essential to take into account the fact that problems in spatial memory and navigation should arise from the alteration of the close links between the cingulum bundle and brain sites known to contribute to spatial processes [86]. Previous studies determined already the presence of cognitive dysfunctions in migraine patients related to visuospatial abilities [87]. It is interesting to note that Messina et al [87] noticed an aspecific and punctate white matter hyperintensity in the cingulum area for migraine patients. Although no differences in the volume of WM hyperintensities (WMH) have been registered between controls and migraineurs [87]. As mentioned before, a decrease of CSF volume has been registered in that area. Thus, it is possible to assume that the WM volume could increase consequentially. It is possible to suspect that an increase in the intracellular space in the cingulum could also lead to alterations related to the visual-spatial abilities of menstrual migraine patients.

Regarding the SLF, this is part of the longitudinal association fiber system, which lays several connections between the frontal lobe and the other areas of the ipsilateral hemisphere [88]. Together with the Arcuate Fasciculus (AF), these play a major role in speech and language [89]. Particularly, the left SLF has been consistently associated with language processing, due to the fact that it connects Broca's and Wernicke's areas [90]. As shown in Masson et al [90], migraine cannot be considered strongly associated with major language defects. Although some neuropsychological differences in language performance between control and migraineurs were detected [90]. Specifically, a decreased WM volume has been detected in migraineurs' left superior longitudinal fasciculus (compared to controls), which could explain the slight dysfunction that migraineurs can present regarding language performances. However, according to the TBSS analysis performed in our research work, an opposite result has been found (decreased values of CSF volume in migraineurs' left SLF, hence, expected increment of WM and GM volumes in that area). Further investigations are required in order to clarify this topic.

As it is possible to visualize in the results section, the frontal major was the area in

which the voxels with the smallest p-values were detected. This area is a white matter fiber bundle, aims to connect the occipital lobes and cross the midline via the splenium of the corpus callosum [91]. In previous studies, it has been shown that an alteration of the white matter bundle in the frontal major could be associated with the frequency of migraine attacks [69, 92]. Even if the aforementioned studies [69, 92] reported some alterations in this area, the specific function of the tract is not fully known.

Regarding the IFOF, this white matter tract is described as the longest associative bundle in the human brain and it connects several parts of the temporo-basal area, occipital cortex, and superior parietal lobule to the frontal lobe through the external/extreme capsule complex [92]. Both anatomical definition and exact functional role of the IFOF are still under debate. Although it is thought that IFOF could be related to the semantic processing for reading and writing [69]. Some variations in terms of MD have been found in this area in the pediadric migraine study conducted by Messina et al [93]. The MD values for this tract was lower than the health control. MD is defined as the measure of average molecular motion that is independent of any tissue-based directionality [94]. Thus, with a low value of MD, the average molecular motion will be less as well, indicating less presence of water. In this sense, the results related to IFOF in our work should be consistent with the results found by Messina et al [93].
Also in Álvaro Planchuelo-Gómez et al [70], some variations of the parameter RTOP were discovered in IFOF with the application of AMURA model. Indeed, in the mentioned study, EM patients presented lower values of RTOP in this tract compared to healthy controls. RTOP is defined as the probability for molecules to undergo no net displacement between the application of the two diffusion sensitizing gradients [95]. If RTOP assumes low values, this means that the probability of the single molecule to return to its original position after a space displacement is low. Hence, the space displacement performed by the molecule should be considered too wide and, for this reason, it won't be easy for the molecule to return to its original position. Therefore, lower RTOP values indicate a higher average molecular motion and, hence, higher MD values. In our case, lower ISOVF values have been found in EM patients compared to controls in this tract. As mentioned before, lower ISOVF values indicate lower MD values. This can be considered as an opposite result compared to the one obtained by Álvaro Planchuelo-Gómez et al [70] due to the fact that they found lower RTOP values in IFOF for EM patients compared to controls, indicating higher MD values for EM patients.

6.2. Discussion of the ROI analysis results

In this study, a ROI analysis has been conducted in the 10 WM tracts that had been selected in the previous TBSS analysis. The ROI analysis revealed significant differences in just 5 WM tracts, which are the left splenium of Corpus callosum (CC), left ATR, left IFOF and left SLF in the comparison between MM for the ISOVF parameter in the comparison between MM patients and healthy controls.

Starting to analyze the Splenium of CC, this is defined as the most posterior and thickest portion of the CC and it consists of several axonal fibers that serve to connect occipital, temporal, posterior, and parietal cortices [96]. The specific function of this WM structure is still not well known. Moreover, some clinical signs could be associated with an alteration of the splenium of CC, such as seizure, dysarthria, confusion, and ataxia [96].
Both Yu et al. and Messina et al. [93, 97] reported an alteration of the splenium of CC. In particular, a decrease in MD values has been reported in the comparison between EM patients and healthy controls. As mentioned before, a low value of MD could suggest a lower presence of water. A low value of ISOVF also implies a lower presence of water due to the fact that this parameter is measuring the volume fraction of the CSF in a particular voxel. Thus, the results that we found for this WM tract were consistent with the aforementioned studies.

The ATR is an WM fiber bundle that connects the thalamus and prefrontal cortex via the interior limb of the internal capsule ([98]). Furthermore, this tract is involved in planning complex behaviors and executive functions.
In this WM tract, neither Planchuelo-Gómez et al. [68] nor Neeb et al. [67] found a significant difference between EM migraine and healthy controls. Although our results revealed a decrease in the CSF volume (decrease of ISOVF values) in the EM patients compared to the controls in the left ATR.

Regarding the PCR, this is the posterior part of the Corona Radiata, which is a collection of nerve fibers present in the brain. This WM structure carries messages between the brain cells of the brain stem and the cerebral cortex. Both of them are related to behaviors connected to sensation and motor function. [99].
No significant difference between EM patients and healthy controls has been found in Planchuelo-Gómez et al. [68] for this structure. Although our results displayed a decrease in ISOVF values for the EM patients compared to controls (midcycle-interictal comparison).

Furthermore, in this tract, the ROI analysis revealed another significant difference in the ISOVF values also in the comparison between controls under the midcycle phase and under the premenstrual phase. Since we're not interested in comparisons among controls, this result could be considered "non-relevant" for our purposes.

Talking about the SLF, it is possible to see in this tract a significant increase of ISOVF values in EM patients under the postictal phase compared to the controls under the premenstrual phase. Messina et al. [93] also revealed a significant alteration of this tract. Specifically, they registered a decrease in MD values in migraine patients compared to controls. As explained before, decreases in MD values could be associated with a loss of CSF. In our case, we registered an increase in the CSF volume in this area for the EM patients (increase of ISOVF values). Therefore, our results are in contrast to the ones obtained in the aforementioned study.

Finally, the results obtained for the IFOF are fully consistent with the ones obtained with the TBSS analyiss.

6.3. Comparison between TBSS analysis and ROI analysis results

Surprisingly, the results obtained from the ROI analysis revealed consistency just for the left IFOF. Indeed, we registered a significant decrease in the ISOVF parameter in MM patients under the interictal phase compared to the controls under the midcycle phase, which is the same result obtained with the previous TBSS analysis.

A significant difference was found with the ROI analysis in left Cingulum and left Forceps Major for any comparison and parameter. Therefore, for these WM tracts, we detected a decrease in sensitivity and the results revealed a strong inconsistency, as we registered in the previous voxelwise approach significant differences for ISOVF in the comparison midcycle-interictal for both of the aforementioned tracts.

Regarding the left SLF, the ROI analysis revealed significant differences for ISOVF in the midcycle-premenstrual and premenstrual-posictal comparisons, instead of in the midcycle-interictal comparison as obtained in the TBSS analysis.

Furthermore, some WM tracts revealed significant differences that were not registered

with the TBSS analysis, such as the left splenium of corpus callosum, left ATR and left PCR.

7 | Conclusion

In this study, a whole-brain white-matter tracts analysis has been conducted at first using the TBSS analysis between different groups of subjects. The only relevant white-matter alterations were found in the comparison between the midcycle phase of the control subjects and the interictal phase of the episodic migraine patients just for the ISOVF parameter. These alterations have been found in left inferior fronto-occipital fasciculus, left forceps major, left superior longitudinal fasciculus, and left cingulum (with a threshold of 0.05 for the p-value). No significant differences between controls and migraineurs have been detected for the ICVF (intracellular volume fraction) parameter.

Based on the results obtained by the TBSS analysis, 10 WM tracts have been selected to deeply investigate potential significant differences among groups. The ROI analysis revealed significant differences in just 5 WM tracts, which are the left splenium of CC, left ATR, left IFOF and left SLF for the ISOVF parameter in the comparison between MM patients and healthy controls.

To conclude, it is possible to state that generally the results that were found with the ROI analysis are inconsistent with respect to the ones obtained with the TBSS analysis. Although the TBSS definitely helped the author to understand what potential areas could be subjected to an alteration caused by migraine. Thus, it has been possible to limit our research to some specific ROIs, reducing the total number of performed statistical tests. This could be essential in terms of reduction of the Type 1 error, which is related to the false-positive results as mentioned in subchapter 4.5.1.

It is very important to take into account the fact that it is not fully certain that the NODDI model could be the most suitable one for the case of episodic migraine. Even if the AMICO framework could strongly reduce the fitting time of NODDI, the time required for all the processes is still higher than the DTI model, and, hence, this could limit the investigation.

Moreover, a large dataset should be required in order to investigate deeply the alteration of the whole-brain white-matter tracts in menstrual migraine. Hence, the limited sample size analyzed in this study could be seen as a strong limitation of the present study.

Bibliography

[1] Y. Zhang, Q. Kong, J. Chen, L. Li, D. Wang, and J. Zhou, "International classification of headache disorders 3rd edition beta-based field testing of vestibular migraine in china: Demographic, clinical characteristics, audiometric findings and diagnosis statues," *Cephalalgia*, vol. 36, no. 3, pp. 240–248, SAGE Publications Sage UK: London, England, doi: 10.1177/0333102413485658, 2016.

[2] H. C. C. of the International Headache Society (IHS), "The international classification of headache disorders, (beta version)," *Cephalalgia*, vol. 33, no. 9, pp. 629–808, Sage Publications Sage UK: London, England. Crossref, https://doi.org/10.1177/0333102413485658, 2013.

[3] V. K. Gupta, "Pathophysiology of migraine: an increasingly complex narrative to 2020," *Future Neurology*, vol. 14, no. 2, p. FNL12, https://doi.org/10.2217/fnl-2019-0003, 2019.

[4] L. M. Cupini, I. Corbelli, and P. Sarchelli, "Menstrual migraine: what it is and does it matter?," *Journal of Neurology*, vol. 268, no. 7, pp. 2355–2363, Springer Science and Business Media LLC, https://doi.org/10.1007/s00415-020-09726-2, 2021.

[5] C. L. Rae, G. Davies, S. N. Garfinkel, M. C. Gabel, N. G. Dowell, M. Cercignani, A. K. Seth, K. E. Greenwood, N. Medford, H. D. Critchley, and et al., "Deficits in neurite density underlie white matter structure abnormalities in first-episode psychosis," *Biological Psychiatry*, vol. 82, no. 10, p. 716–725, https://doi.org/10.1016/j.biopsych.2017.02.008, 2017.

[6] C. F. Slattery, J. Zhang, R. W. Paterson, A. J. Foulkes, A. Carton, K. Macpherson, L. Mancini, D. L. Thomas, M. Modat, N. Toussaint, and et al., "Apoe influences regional white-matter axonal density loss in alzheimer's disease," *Neurobiology of Aging*, vol. 57, p. 8–17, https://doi.org/10.1016/j.neurobiolaging.2017.04.021, 2017.

[7] G. P. Winston, C. Micallef, M. R. Symms, D. C. Alexander, J. S. Duncan, and H. Zhang, "Advanced diffusion imaging sequences could aid assessing patients with

focal cortical dysplasia and epilepsy," *Epilepsy Research*, vol. 108, no. 2, p. 336–339, doi: 10.1016/j.eplepsyres.2013.11.004, 2014.

[8] K. Kamagata, T. Hatano, A. Okuzumi, Y. Motoi, O. Abe, K. Shimoji, K. Kamiya, M. Suzuki, M. Hori, K. K. Kumamaru, and et al., "Neurite orientation dispersion and density imaging in the substantia nigra in idiopathic parkinson disease," *European Radiology*, vol. 26, no. 8, p. 2567–2577, doi: 10.1007/s00330-015-4066-8, 2015.

[9] J. Zhang, S. Gregory, R. I. Scahill, A. Durr, D. L. Thomas, S. Lehericy, G. Rees, S. J. Tabrizi, and H. Zhang, "In vivo characterization of white matter pathology in premanifest huntington's disease," *Annals of Neurology*, vol. 84, no. 4, p. 497–504, doi: 10.1002/ana.25309, 2018.

[10] K. Floyd, A. Eberly, and M. Hadjifrangiskou, "Adhesion of bacteria to surfaces and biofilm formation on medical devices," in *Biofilms and implantable medical devices, Vanderbilt University Medical Center, Nashville, TN, United States*, pp. 47–95, Elsevier, https://doi.org/10.1016/B978-0-08-100382-4.00003-4, 2017.

[11] R. Brown, "Xxvii. a brief account of microscopical observations made in the months of june, july and august 1827, on the particles contained in the pollen of plants; and on the general existence of active molecules in organic and inorganic bodies," *The philosophical magazine*, vol. 4, no. 21, Taylor & Francis, pp. 161–173, https://doi.org/10.1080/14786442808674769, 1828.

[12] V. Singh, "Albert einstein: His annus mirabilis 1905," *arXiv preprint physics/0701240*, https://doi.org/10.48550/arXiv.physics/0701240, 2007.

[13] W. S. Price, "Pulsed-field gradient nuclear magnetic resonance as a tool for studying translational diffusion: Part 1. basic theory," *Concepts in Magnetic Resonance: An Educational Journal*, vol. 9, no. 5, pp. 299–336, Wiley Online Library, https://doi.org/10.1002/(sici)1099-0534(1997)9:5299::aid-cmr2 3.0.co;2-u, 1997.

[14] D. Le Bihan, "Diffusion mri: what water tells us about the brain," *EMBO molecular medicine*, vol. 6, no. 5, pp. 569–573, https://doi.org/10.1002/emmm.201404055, 2014.

[15] J. Zhang, *Applications of NODDI for imaging in vivo white matter pathology in neurodegenerative diseases*. PhD thesis, UCL (University College London), https://discovery.ucl.ac.uk/id/eprint/10069329/1/Zhang_10069329_thesis.pdf, 2019.

[16] T. Ai, J. N. Morelli, X. Hu, D. Hao, F. L. Goerner, B. Ager, and V. M. Runge, "A historical overview of magnetic resonance imaging, focusing on technological inno-

vations," *Investigative Radiology,*, vol. 47, no. 12, pp. 725–741, Ovid Technologies (Wolters Kluwer Health), https://doi.org/10.1097/rli.0b013e318272d29f, 2012.

[17] A. Parupudi, S. H. R. Mulagapati, and J. A. Subramony, "Nanoparticle technologies: Recent state of the art and emerging opportunities," *Dosage Form Design and Development, BioPharmaceutical Development, BioPharmaceuticals RD, AstraZeneca, Gaithersburg, MD, United States- Analytical Science, BioPharmaceuticals Development, RD, AstraZeneca, Gaithersburg, MD, United States- Biologics Engineering, RD, AstraZeneca, Gaithersburg, MD, United StatesNanoparticle Therapeutics*, pp. 3–46, Elsevier, https://doi.org/10.1016/B978-0-12-820757-4.00009-0, 2022.

[18] P. C. Lauterbur, "Image formation by induced local interactions: examples employing nuclear magnetic resonance," *Nature*, vol. 242, no. 5394, pp. 190–191, Springer Science and Business Media LLC, https://doi.org/10.1038/242190a0, 1973.

[19] S. Huettel, A. Song, and G. McCarthy, *Functional Magnetic Resonance Imaging*. Sinauer, ISBN: 9780878936274, lccn: 2014025114, https://books.google.pt/books?id=CUrVoAEACAAJ, 2014.

[20] D. Sinnaeve, "The stejskal–tanner equation generalized for any gradient shape—an overview of most pulse sequences measuring free diffusion," *Concepts in Magnetic Resonance Part A*, vol. 40, no. 2, pp. 39–65, Wiley Online Library, https://doi.org/10.1002/cmr.a.21223, 2012.

[21] J. Hennig, "K-space sampling strategies," *European radiology*, vol. 9, no. 6, Springer Science and Business Media LLC, pp. 1020–1031, 1999. Crossref, https://doi.org/10.1007/s003300050788.

[22] M. Čuperlović-Culf, *NMR metabolomics in cancer research*. Elsevier Science, isbn: 9781908818263, lccn: 2012946843, Woodhead Publishing Series in Biomedicine, Elsevier Science, https://books.google.pt/books?id=XYtwAgAAQBAJ, 2012.

[23] F. Schmitt, M. K. Stehling, and R. Turner, *Echo-planar imaging: theory, technique and application*. isbn: 9783642804458, Springer Science & Business Media, https://books.google.pt/books?id=Etv5ngEACAAJ, 2012.

[24] E. O. Stejskal and J. E. Tanner, "Spin diffusion measurements: spin echoes in the presence of a time-dependent field gradient," *The journal of chemical physics*, vol. 42, no. 1, American Institute of Physics, pp. 288–292, https://doi.org/10.1063/1.1695690, 1965.

[25] A. W. Toga, *Brain mapping: An encyclopedic reference*. Academic Press, isbn: 9780123973160, https://books.google.pt/books?id=ysucBAAAQBAJ, 2015.

[26] B. Kaya and Z. Koc, "Diffusion-weighted mri and optimal b-value for characterization of liver lesions," *Acta Radiologica*, vol. 55, no. 5, pp. 532–542, SAGE Publications Sage UK: London, England, https://doi.org/10.1177/0284185113502017, 2014.

[27] L. J. O'Donnell and C.-F. Westin, "An introduction to diffusion tensor image analysis," *Neurosurgery Clinics*, vol. 22, no. 2, pp. 185–196, Elsevier BV, https://doi.org/10.1016/j.nec.2010.12.004, 2011.

[28] P. Mukherjee, J. Berman, S. W. Chung, C. Hess, and R. Henry, "Diffusion tensor mr imaging and fiber tractography: theoretic underpinnings," *American journal of neuroradiology*, vol. 29, no. 4, pp. 632–641, doi: 10.3174/ajnr.A1051, Am Soc Neuroradiology, 2008.

[29] H. Zhang, P. L. Hubbard, G. J. Parker, and D. C. Alexander, "Axon diameter mapping in the presence of orientation dispersion with diffusion mri," *Neuroimage*, vol. 56, no. 3, pp. 1301–1315, Elsevier BV, https://doi.org/10.1016/j.neuroimage.2011.01.084, 2011.

[30] K. H. Karlsgodt, T. Rosser, E. S. Lutkenhoff, T. D. Cannon, A. Silva, and C. E. Bearden, "Alterations in white matter microstructure in neurofibromatosis-1," doi: 10.1371/journal.pone.0047854, Public Library of Science San Francisco, USA, 2012.

[31] R. Fick, "Advanced dmri signal modeling for tissue microstructure characterization," Université Côte d'Azur, 2017.

[32] H. Zhang, T. Schneider, C. A. Wheeler-Kingshott, and D. C. Alexander, "Noddi: practical in vivo neurite orientation dispersion and density imaging of the human brain," *Neuroimage*, vol. 61, no. 4, pp. 1000–1016, Elsevier BV, https://doi.org/10.1016/j.neuroimage.2012.03.072, 2012.

[33] M. Abramowitz and I. A. Stegun, "Handbook of mathematical functions with formulas, graphs, and mathematical tables," in *Technometrics, vol. 7, no. 1, JSTOR, p. 78. Crossref, https://doi.org/10.2307/1266136*, 1965.

[34] P. M. Macey, M. A. Thomas, and L. A. Henderson, "Dti-based upper limit of voxel free water fraction," *Heliyon*, vol. 4, no. 7, p. e00700, Elsevier BV, https://doi.org/10.1016/j.heliyon.2018.e00700, 2018.

[35] N. V. Kraguljac, M. Guerreri, M. J. Strickland, and H. Zhang, "Neurite orientation dispersion and density imaging in psychiatric disorders: A systematic liter-

ature review and a technical note," *Biological Psychiatry: Global Open Science*, https://doi.org/10.1371/journal.pone.0047854, Elsevier, 2022.

[36] D. K. Jones, T. R. Knösche, and R. Turner, "White matter integrity, fiber count, and other fallacies: the do's and don'ts of diffusion mri," *Neuroimage*, vol. 73, pp. 239–254, Elsevier BV, https://doi.org/10.1016/j.neuroimage.2012.06.081, 2013.

[37] A. W. Chung, K. K. Seunarine, and C. A. Clark, "Noddi reproducibility and variability with magnetic field strength: a comparison between 1.5 t and 3 t," *Human brain mapping*, vol. 37, no. 12, pp. 4550–4565, Wiley Online Library, https://doi.org/10.1002/hbm.23328, 2016.

[38] K. J. Friston and J. Ashburner, "Generative and recognition models for neuroanatomy," *Neuroimage*, vol. 23, no. 1, pp. 21–24, Academic Press, https://doi.org/10.1016/j.neuroimage.2004.04.021, 2004.

[39] H.-J. Park, C.-F. Westin, M. Kubicki, S. E. Maier, M. Niznikiewicz, A. Baer, M. Frumin, R. Kikinis, F. A. Jolesz, R. W. McCarley, and et al., "White matter hemisphere asymmetries in healthy subjects and in schizophrenia: A diffusion tensor mri study," *NeuroImage*, vol. 23, no. 1, p. 213–223, Elsevier BV, https://doi.org/10.1016/j.neuroimage.2004.04.036, 2004.

[40] S. M. Smith, M. Jenkinson, H. Johansen-Berg, D. Rueckert, T. E. Nichols, C. E. Mackay, K. E. Watkins, O. Ciccarelli, M. Z. Cader, P. M. Matthews, and et al., "Tract-based spatial statistics: Voxelwise analysis of multi-subject diffusion data," *NeuroImage*, vol. 31, no. 4, p. 1487–1505, Elsevier BV, https://doi.org/10.1016/j.neuroimage.2006.02.024, 2006.

[41] A. V. Faria, J. Zhang, K. Oishi, X. Li, H. Jiang, K. Akhter, L. Hermoye, S.-K. Lee, A. Hoon, E. Stashinko, and et al., "Atlas-based analysis of neurodevelopment from infancy to adulthood using diffusion tensor imaging and applications for automated abnormality detection," *NeuroImage*, vol. 52, no. 2, p. 415–428, Elsevier BV, f, https://doi.org/10.1016/j.neuroimage.2010.04.238, 2010.

[42] Q. B. Institute, "Types of glia," Queensland Brain Institute - University of Queensland, https://qbi.uq.edu.au/brain-basics/brain/brain-physiology/types-glia, Jun 2017.

[43] B. Blaus, "Medical gallery of blausen medical 2014," *WikiJournal of Medicine*, vol. 1, no. 2, doi: 10.15347/wjm/2014.010, 2014.

[44] M. Colleen Doherty, "The anatomy of the myelin sheath, the function and dysfunc-

tion of nerve insulation," Verywell Health, https://www.verywellhealth.com/myelin-sheath-4129059, Feb 2022.

[45] B. B. Editors and B. Editors, "Myelin sheath - definition and function," https://biologydictionary.net/myelin-sheath/, Mar 2019.

[46] E. Syková and C. Nicholson, "Diffusion in brain extracellular space," *Physiological Reviews*, vol. 88, no. 4, p. 1277–1340, 10.1152/physrev.00027.2007, 2008.

[47] H. Nonaka, M. Akima, T. Hatori, T. Nagayama, Z. Zhang, and F. Ihara, "The microvasculature of the cerebral white matter: Arteries of the subcortical white matter," *Journal of Neuropathology amp; Experimental Neurology*, vol. 62, no. 2, p. 154–161, Oxford University Press (OUP), https://doi.org/10.1093/jnen/62.2.154, 2003.

[48] D. Le Bihan, E. Breton, D. Lallemand, M. L. Aubin, J. Vignaud, and M. Laval-Jeantet, "Separation of diffusion and perfusion in intravoxel incoherent motion mr imaging.," *Radiology*, vol. 168, no. 2, p. 497–505, Radiological Society of North America (RSNA), https://doi.org/10.1148/radiology.168.2.3393671, 1988.

[49] U. Themes and drzezo, "White matter anatomy," Radiology Key, https://radiologykey.com/white-matter-anatomy/, Mar 2017.

[50] WHO, "Headache disorders," World Health Organization, https://www.who.int/en/news-room/fact-sheets/detail/headache-disorders, Apr 2016.

[51] J. Olesen, "International classification of headache disorders," *The Lancet Neurology*, vol. 17, no. 5, p. 396–397, Epub, doi: 10.1016/s1474-4422(18)30085-1, 2018.

[52] B. Colombo and M. Filippi, "Migraine and literature: A narrative historical review," *Neurological Sciences*, vol. 42, no. 2, p. 565–569, Springer Science and Business Media LLC, https://doi.org/10.1007/s10072-020-05014-z, 2021.

[53] J. Olesen, "The international classification of headache disorders. 2nd edition (ichd-ii)," *Revue Neurologique*, vol. 161, no. 6-7, p. 689–691, Elsevier BV, https://doi.org/10.1016/s0035-3787(05)85119-7, 2005.

[54] A. M. Foundation, "The timeline of a migraine attack," url: https://americanmigrainefoundation.org/resource-library/timeline-migraine-attack/, Jan 2018.

[55] J. Herndon, "Migraine stages: Prodrome, aura, headache, and postrome," Healthline Media, url: https://www.healthline.com/health/migraine-stages, Apr 2021.

[56] F. Frankandmaven, "Episodic vs. chronic migraine - what is the difference?," Clinvest Research, https://clinvest.com/episodic-vs-chronic-migraine-what-is-the-difference, Sep 2021.

[57] T. M. Trust, "Menstrual migraine," The Migraine Trust, https://migrainetrust.org/understand-migraine/types-of-migraine/menstrual-migraine/, Nov 2021.

[58] T. Ansari, A. M. Lagman-Bartolome, D. Monsour, and C. Lay, "Management of menstrual migraine," *Current Neurology and Neuroscience Reports*, vol. 20, no. 10, Springer Science and Business Media LLC, https://doi.org/10.1007/s11910-020-01067-x, 2020.

[59] A. Blumenfeld, S. Varon, T. Wilcox, D. Buse, A. Kawata, A. Manack, P. Goadsby, and R. Lipton, "Disability, hrqol and resource use among chronic and episodic migraineurs: Results from the international burden of migraine study (ibms)," *Cephalalgia*, vol. 31, no. 3, p. 301–315, SAGE Publications, https://doi.org/10.1177/0333102410381145, 2010.

[60] D. C. Buse, A. Manack, D. Serrano, C. Turkel, and R. B. Lipton, "Sociodemographic and comorbidity profiles of chronic migraine and episodic migraine sufferers," *Journal of Neurology, Neurosurgery amp; Psychiatry*, vol. 81, no. 4, p. 428–432, BMJ, https://doi.org/10.1136/jnnp.2009.192492, 2010.

[61] M. E. Bigal, D. Serrano, M. Reed, and R. B. Lipton, "Chronic migraine in the population: Burden, diagnosis, and satisfaction with treatment," *Neurology*, vol. 71, no. 8, p. 559–566, Ovid Technologies (Wolters Kluwer Health), https://doi.org/10.1212/01.wnl.0000323925.29520.e7, 2008.

[62] Z. Katsarava, D. C. Buse, A. N. Manack, and R. B. Lipton, "Defining the differences between episodic migraine and chronic migraine," *Current Pain and Headache Reports*, vol. 16, no. 1, p. 86–92, Springer Science and Business Media LLC, https://doi.org/10.1007/s11916-011-0233-z, 2011.

[63] M. C. Kruit, L. J. Launer, M. A. van Buchem, G. M. Terwindt, and M. D. Ferrari, "Migraine as a risk factor for white matter lesions, silent infarctions, and ischemic stroke: The evidence for a link," *Headache Currents*, vol. 2, no. 3, p. 62–70, Wiley, May 2005, https://doi.org/10.1111/j.1743-5013.2005.20309.x, 2005.

[64] A. Porter, J. P. Gladstone, and D. W. Dodick, "Migraine and white matter hyperintensities," *Current Pain and Headache Reports*, vol. 9, no. 4, p. 289–293, Springer Science and Business Media LLC, https://doi.org/10.1007/s11916-005-0039-y, 2005.

[65] A. G. Hamedani, K. M. Rose, B. L. Peterlin, T. H. Mosley, L. H. Coker, C. R. Jack, D. S. Knopman, A. Alonso, and R. F. Gottesman, "Migraine and white matter hyperintensities: The aric mri study," *Neurology*, vol. 81, no. 15, p. 1308–1313, Ovid Technologies (Wolters Kluwer Health), https://doi.org/10.1212/wnl.0b013e3182a8235b, 2013.

[66] C. D. Chong and T. J. Schwedt, "Migraine affects white-matter tract integrity: A diffusion-tensor imaging study," *Cephalalgia*, vol. 35, no. 13, p. 1162–1171, SAGE Publications, https://doi.org/10.1177/0333102415573513, 2015.

[67] L. Neeb, K. Bastian, K. Villringer, H. C. Gits, H. Israel, U. Reuter, and J. B. Fiebach, "No microstructural white matter alterations in chronic and episodic migraineurs: a case–control diffusion tensor magnetic resonance imaging study," *Headache: The Journal of Head and Face Pain*, vol. 55, no. 2, pp. 241–251, Wiley Online Library, https://doi.org/10.1111/head.12496, 2015.

[68] Á. Planchuelo-Gómez, D. García-Azorín, Á. L. Guerrero, S. Aja-Fernández, M. Rodríguez, and R. de Luis-García, "White matter changes in chronic and episodic migraine: a diffusion tensor imaging study," *The journal of headache and pain*, vol. 21, no. 1, pp. 1–15, Springer Science and Business Media LLC, https://doi.org/10.1186/s10194-019-1071-3, 2020.

[69] R. Rahimi, M. Dolatshahi, F. Abbasi-Feijani, S. Momtazmanesh, G. Cattarinussi, M. H. Aarabi, and L. Pini, "Microstructural white matter alterations associated with migraine headaches: a systematic review of diffusion tensor imaging studies," *Brain Imaging and Behavior*, pp. 1–27, Springer Science and Business Media LLC, https://doi.org/10.1007/s11682-022-00690-1, 2022.

[70] Á. Planchuelo-Gómez, D. García-Azorín, Á. L. Guerrero, R. de Luis-García, M. Rodríguez, and S. Aja-Fernández, "Alternative microstructural measures to complement diffusion tensor imaging in migraine studies with standard mri acquisition," *Brain Sciences*, vol. 10, no. 10, p. 711, MDPI, doi: 10.1007/s00234-015-1603-8, 2020.

[71] K. Ito, M. Kudo, M. Sasaki, A. Saito, F. Yamashita, T. Harada, S. Yokosawa, I. Uwano, H. Kameda, and Y. Terayama, "Detection of changes in the periaqueductal gray matter of patients with episodic migraine using quantitative diffusion kurtosis imaging: preliminary findings," *Neuroradiology*, vol. 58, no. 2, pp. 115–120, Springer, doi: 10.1007/s00234-015-1603-8, 2016.

[72] A. Chamseddine and M. Sawan, "Deep learning based method for output regular-

ization of the seizure prediction classifier," in *2018 IEEE Life Sciences Conference (LSC)*, pp. 118–121, IEEE, doi:10.1109/LSC.2018.8572221, 2018.

[73] E. B. Assi, D. K. Nguyen, S. Rihana, and M. Sawan, "Towards accurate prediction of epileptic seizures: A review," *Biomedical Signal Processing and Control*, vol. 34, pp. 144–157, Elsevier BV, https://doi.org/10.1016/j.bspc.2017.02.001, 2017.

[74] Z. Wang, J. Yang, and M. Sawan, "A novel multi-scale dilated 3d cnn for epileptic seizure prediction," *2021 IEEE 3rd International Conference on Artificial Intelligence Circuits and Systems (AICAS)*, doi: 10.1109/aicas51828.2021.9458571, 2021.

[75] H.-J. Chen, Y.-Q. Gao, C.-H. Che, H. Lin, and X.-L. Ruan, "Diffusion tensor imaging with tract-based spatial statistics reveals white matter abnormalities in patients with vascular cognitive impairment," *Frontiers in Neuroanatomy*, vol. 12, p. 53, Frontiers Media SA, https://doi.org/10.3389/fnana.2018.00053, 2018.

[76] H. Zhang, "Noddi matlab toolbox," Microstructure Imaging Group | NODDI Matlab toolbox, http://mig.cs.ucl.ac.uk/index.php?n=Tutorial.NODDImatlab, 2021.

[77] A. Daducci, E. J. Canales-Rodríguez, H. Zhang, T. B. Dyrby, D. C. Alexander, and J.-P. Thiran, "Accelerated microstructure imaging via convex optimization (amico) from diffusion mri data," *NeuroImage*, vol. 105, p. 32–44, Elsevier BV, https://doi.org/10.1016/j.neuroimage.2014.10.026, 2015.

[78] A. Daducci, "Fitting the noddi model · daducci/amico wiki," GitHub, https://github.com/daducci/AMICO/wiki/Fitting-the-NODDI-model, 2021.

[79] F. FslWIki, "Contents," TBSS/UserGuide - FslWiki, https://fsl.fmrib.ox.ac.uk/fsl/fslwiki/TBSS/UserGuide, 2021.

[80] R. A. Poldrack, "Region of interest analysis for fmri," *Social cognitive and affective neuroscience*, vol. 2, no. 1, pp. 67–70, Oxford University Press, https://doi.org/10.1093/scan/nsm006, 2007.

[81] M. Froeling, P. Pullens, and A. Leemans, "Dti analysis methods: region of interest analysis," in *Diffusion tensor imaging*, pp. 175–182, doi: 10.1007/978–1–4939–3118–7_9, Springer, 2016.

[82] A. Banerjee, U. Chitnis, S. Jadhav, J. Bhawalkar, and S. Chaudhury, "Hypothesis testing, type i and type ii errors," *Industrial psychiatry journal*, vol. 18, no. 2, p. 127, Wolters Kluwer–Medknow Publications, doi: 10.4103/0972-6748.62274, 2009.

[83] "Templates and atlases included with fsl, atlases - fslwiki."

[84] R. J. Theilmann, J. D. Reed, D. D. Song, M. X. Huang, R. R. Lee, I. Litvan, and D. L. Harrington, "White-matter changes correlate with cognitive functioning in parkinson's disease," *Frontiers in Neurology*, vol. 4, doi: 10.3389/fneur.2013.00037, 2013.

[85] E. J. Bubb, C. Metzler-Baddeley, and J. P. Aggleton, "The cingulum bundle: Anatomy, function, and dysfunction," *Neuroscience amp; Biobehavioral Reviews*, vol. 92, p. 104–127, Elsevier BV, https://doi.org/10.1016/j.neubiorev.2018.05.008, 2018.

[86] J. Zhang, S. Gregory, R. I. Scahill, A. Durr, D. L. Thomas, S. Lehericy, G. Rees, S. J. Tabrizi, and H. Zhang, "In vivo characterization of white matter pathology in premanifest huntington's disease," *Annals of Neurology*, vol. 84, no. 4, p. 497–504, Wiley, https://doi.org/10.1002/ana.25309, 2018.

[87] R. Messina, A. Meani, G. C. Riccitelli, B. Colombo, M. Filippi, and M. A. Rocca, "Neural correlates of visuospatial processing in migraine: Does the pain network help?," *Molecular Psychiatry*, vol. 26, no. 11, p. 6599–6608, Springer Science and Business Media LLC, https://doi.org/10.1038/s41380-021-01085-2, 2021.

[88] F. Janelle, C. Iorio-Morin, S. D'amour, and D. Fortin, "Superior longitudinal fasciculus: A review of the anatomical descriptions with functional correlates," *Frontiers in Neurology*, vol. 13, Frontiers Media SA, https://doi.org/10.3389/fneur.2022.794618, 2022.

[89] K. Chaichana and Q.-H. Alfredo, *Comprehensive overview of modern surgical approaches to intrinsic brain tumors*. London, UK, Elsevier/Academic Press, isbn: 9780128117835, English (US), 488, 2019.

[90] R. Masson, G. Demarquay, D. Meunier, Y. Lévêque, S. Hannoun, A. Bidet-Caulet, and A. Caclin, "Is migraine associated to brain anatomical alterations? new data and coordinate-based meta-analysis," *Brain Topography*, vol. 34, no. 3, p. 384–401, Epub, doi: 10.1007/s10548-021-00824-6, 2021.

[91] P. Driscoll, "Gray's anatomy, 39th edition," *Emergency Medicine Journal*, vol. 23, no. 6, p. 492–492, Emerg Med J, doi: 10.1136/emj.2005.027847, 2006.

[92] C. D. Chong, J. Peplinski, V. Berisha, K. Ross, and T. J. Schwedt, "Differences in fibertract profiles between patients with migraine and those with persistent post-traumatic headache," *Cephalalgia*, vol. 39, no. 9, p. 1121–1133, Pubmed, https://doi.org/10.1177/0333102418815650, 2019.

[93] R. Messina, M. A. Rocca, B. Colombo, E. Pagani, A. Falini, G. Comi, and M. Filippi, "White matter microstructure abnormalities in pediatric migraine patients," *Cephalalgia*, vol. 35, no. 14, pp. 1278–1286, SAGE Publications Sage UK: London, https://doi.org/10.1007/s11682-022-00690-1, 2015.

[94] W. B. Pope, "Brain metastases: neuroimaging," *Handbook of clinical neurology*, vol. 149, pp. 89–112, Elsevier, doi: 10.1016/B978-0-12-811161-1.00007-4, 2018.

[95] E. Özarslan, C. G. Koay, T. M. Shepherd, M. E. Komlosh, M. O. İrfanoğlu, C. Pierpaoli, and P. J. Basser, "Mean apparent propagator (map) mri: a novel diffusion imaging method for mapping tissue microstructure," *NeuroImage*, vol. 78, pp. 16–32, Elsevier, doi: 10.1016/j.neuroimage.2013.04.016, 2013.

[96] M. Yu, Y. Zhang, Y. Li, M. Li, W. Li, J. Zhang, Y.-l. Tang, X.-m. Zhang, Z.-g. Yang, Y.-c. Huang, *et al.*, "Splenial lesions of the corpus callosum: disease spectrum and mri findings," *Korean Journal of Radiology*, vol. 18, no. 4, pp. 710–721, The Korean Society of Radiology, doi: 10.3348/kjr.2017.18.4.710, 2017.

[97] D. Yu, K. Yuan, W. Qin, L. Zhao, M. Dong, P. Liu, X. Yang, J. Liu, J. Sun, G. Zhou, *et al.*, "Axonal loss of white matter in migraine without aura: a tract-based spatial statistics study," *Cephalalgia*, vol. 33, no. 1, pp. 34–42, Sage Publications Sage UK: London, England, doi: 10.1177/0333102412466964, 2013.

[98] R. Niida, B. Yamagata, A. Niida, A. Uechi, H. Matsuda, and M. Mimura, "Aberrant anterior thalamic radiation structure in bipolar disorder: a diffusion tensor tractography study," *Frontiers in psychiatry*, vol. 9, p. 522, Frontiers Media SA, doi: 10.3389/fpsyt.2018.00522, 2018.

[99] "Corona radiata, bartleby," Sep 2021.

List of Figures

List of Tables

List of Acronyms

AD	Axial Diffusivity
ADC	Apparent Diffusion Coefficient
AF	Arcuate Fasciculus
AMICO	Accelerated Microstructure Imaging via Convex Optimization
AMURA	Apparent measures using reduced acquisitions
ATR	Anterior thalamic radiation
CC	Corpus callosum
CM	Chronic Migraine
CSF	Cerebrospinal Fluid
DKI	Diffusion Kurtosis Imaging
dMRI	Diffusion Magnetic Resonance Imaging
DTI	Diffusion Tensor Imaging
DWI	Diffusion Weighted Imaging
EEG	Electroencephalogram
EM	Episodic Migraine
EPI	Echo-planar Imaging
FA	Fractional Anisotropy
FSL	FMRIB Software Library
FW	Free water
FWF	Free Water Fraction
GM	Gray Matter

ICHD International Classification of Headache Disorders

ICVF Intracellular Volume Fraction

IFOF Inferior Fronto-Occipital Fasciculus

ISOVF Isotropic Volume Fraction

MD Mean Diffusivity

MK Mean Kurtosis

MM Menstrual Migraine

MRI Magnetic Resonance Imaging

MRM Migraine related to menstruation

NDI Neurite Density Index

NMR Nuclear Magnetic Resonance

NODDI Neurite Orientation Dispersion and Density Imaging

OD Orientation Dispersion

ODI Orientation Dispersion Index

PCR Posterior corona radiata

PGSE Pulsed Gradient Spin-echo

PMM Pure Menstrual Migraine

RA Relative Anisotropy

RD Radial Diffusivity

RF Radiofrequency pulse

ROI Region of interest

RTOP Return-to-origin Probability

SLF Superior Longitudinal Fasciculus

SMS Simultaneous multi-slice

TBSS Tract-Based Spatial Statistics

TE Echo Time

TFCE Threshold-Free Cluster Enhancement

TR Repetition Time

VBA Voxel-Based Analysis

WHO World Health Organization

WM White Matter

WMH White Matter Hyperintensities——

Acknowledgements

I'm glad that my master student period has come to an end. The last 3 years have been extremely challenging for me. Moving from one city to another, moving from one country to another. At the same time, I found my own way to adapt to every situation and context that I've been through. During these years, I've been exposed to so many different cultures, and this has allowed me to be the open-minded and mature person that I wanted to be. Lisbon positively changed my life. The inclusiveness of this city stole my heart since the moment I arrived, and I'll always be thankful for that.

First of all, I would like to acknowledge my dissertation supervisors, Prof. Rita Nunes and Prof. Patricia Figurereiro, for the sharing of knowledge, their insight, and support that has made this thesis possible. Their professionalism and work dedication have inspired me during the entire process. Many thanks as well to the entire LASEEB team for all the technical support that I've received. I would like to acknowledge my supervisor from Politecnico di Milano, Anna Maria Maddalena Bianchi, for the last revision of the work

I would like to thank all the beautiful souls that I met in Portugal. Specifically, I would like to thank all my close friends here. Thank you for the love and the support that I received and I am still receiving from all of you. Even if some of you have already left the country, you will always have a space in my heart.

I would like to thank all my friends from Italy. Thank you for being my biggest fans and believing in my dreams. The warmth that I've been receiving every time I came back home gave me the strength and the energy that I needed to continue living my life at my best.

I would like to thank my family for their encouragement and care over all these years, for always being there for me. I know that the physical distance has been tough for you. It has been the same for me. I'm glad that, at last, mine and your sacrifices have been rewarded. From the bottom of my heart, thank you.